

Integrating kinematic restoration and forward finite element simulations to constrain the evolution of salt diapirism and overburden deformation in evaporite basins

J. Ryan Thigpen^{a,*}, Dan Roberts^b, J. Kent Snow^c, Christopher D. Walker^c, Adam Bere^b

^a Department of Earth and Environmental Sciences, University of Kentucky, Lexington, KY, 40506, USA

^b Rockfield Global, Ethos, Kings Road, Prince of Wales Dock, Swansea Waterfront, SA1 8AS, UK

^c BP America, 501 Westlake Park Boulevard, Houston, TX, 77079, USA

ABSTRACT

In evaporite basins, salt deformation including inflation, diapirism, and salt canopy emplacement is inherently non-coaxial and ductile and thus it presents challenges for two-dimensional kinematic restorations that rely on line-length and area-balancing assumptions. Also, because salt flow and the resulting deformation of adjacent cover units can be driven by temporally and spatially transient salt pressure gradients, kinematic restorations are generally unable to predict the magnitude and distribution of subseismic deformation that results from a particular structural scenario. Here, we use a case study from the Atwater fold belt, Gulf of Mexico, to test a new workflow that involves comparison of kinematic restoration models with forward numerical (finite-element) models of structural evolution to examine the physical validity of solutions derived from the kinematic restorations and to determine the nature and spatial distribution of the resultant subseismic deformation. In the Atwater fold belt, which represents the downdip portion of a linked updip (landward) extensional-downdip (seaward) contractional system, our kinematic restorations indicated that major anticlines likely result from early short wavelength folding followed by (1) inflation of the autochthonous salt to drive failure of the overburden, (2) collapse of the updip limb of the major salt-cored anticline as the salt evacuates updip, and (3) rapid emplacement of the allochthonous salt canopy. In margin scale finite element models of the same system, progradation of the sedimentary wedge above the weak salt substrate leads to basinward migration of the salt and produces inflation of the major downdip salt-cored folds, as predicted by the kinematic model. However, in relatively strong overburden materials (equivalent friction angle = 32°), such salt flow only sustains inflation of the anticlines and is unable to reproduce the interpreted collapse of the anticlinal backlimb or emplacement of the salt canopy. Alternate model runs that include a significant reduction in material strength (equivalent friction angle = 18°) allow salt in the anticlinal crest to drive both reactive and active diapirism and ultimately lead to rapid emplacement of allochthonous canopies. In all of these models, diapirism drives substantial seismically-resolvable and subseismic deformation of wall rocks. Additionally, these models clearly show that the stress field, and particularly the K value (horizontal-vertical stress ratio) of the sediments adjacent to salt structures used for estimating stress magnitudes for drilling predictions, is fundamentally dependent on what point along the evolutionary path from autochthonous salt, to diapir, to salt sheet, that each structure resides. These results highlight the need to test complex kinematic restorations with physics-based techniques. Additionally, they demonstrate that integrating kinematic restorations with these finite element solutions can substantially increase our ability to predict both subseismic reservoir damage in sediments adjacent to salt structures and the K values used for forecasting drilling conditions, particularly in young basins filled with poorly consolidated sediments.

1. Introduction

Many of the world's prolific hydrocarbon provinces lie in passive margin salt basins (e.g., Gulf of Mexico, Persian Gulf, North Sea, Lower Congo, Campos, and Precaspian basins; Hudec and Jackson, 2007; Rowan and Ratliff, 2012) and many major deepwater fields in these basins are influenced by salt structures. Along these evaporite-floored passive margins, gravity driven collapse and basin prograding sedimentation leads to development of an updip extensional zone that is kinematically linked with a downdip contractional system along a common master detachment (Fig. 1; Wu et al., 1990; Demercian et al., 1993; Letouzey et al., 1995; Peel et al., 1995). In the Gulf of Mexico

basin, the genesis of the major deepwater fields is directly tied to salt flow, including diapir evolution. The evolution of these features exerts tremendous influence on the structural geometry of overburden units and the consequent compartmentalization of prospects, the depositional paleobathymetry, and the resultant distribution of lithofacies, which directly drives field developmental planning (i.e., location and number of wells). In these geologically young systems that include poorly consolidated sediments, salt pressure can drive plastic deformation that can be both pervasive (accelerated compaction; Weller, 1959) and discrete (deformation bands; Schultz and Siddharthan, 2005) and lead to unpredicted reservoir flow “baffling”. Additionally, because viscous salt flow rates can result in strain rates much higher (10^{-8} to

* Corresponding author.

E-mail address: ryan.thigpen@uky.edu (J.R. Thigpen).

<https://doi.org/10.1016/j.jsg.2018.10.003>

Received 2 April 2018; Received in revised form 3 October 2018; Accepted 3 October 2018

Available online 06 October 2018

0191-8141/ © 2018 Elsevier Ltd. All rights reserved.

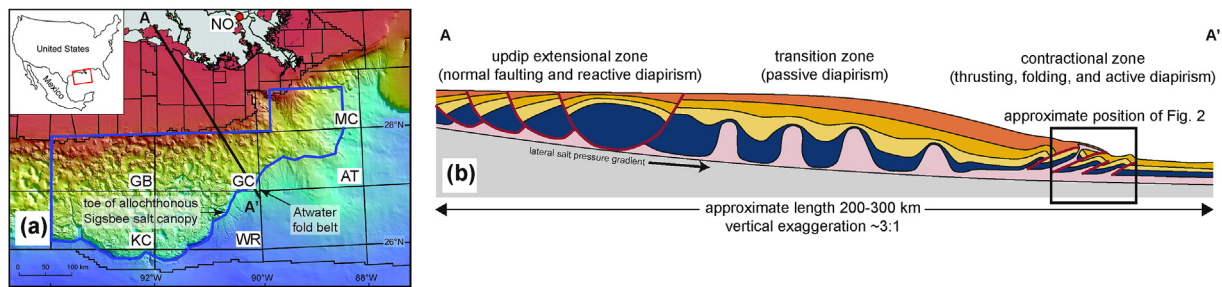


Fig. 1. (a) Bathymetric map of the northern Gulf of Mexico and southernmost onshore Louisiana. Position of section line from Fig. 1b is shown. The Atwater fold belt lies directly beneath the toe of the allochthonous Sigsbee salt canopy, which is clearly expressed in the present-day bathymetry. NO – New Orleans. MC – Mississippi Canyon. AT – Atwater Valley. GC – Green Canyon. WR – Walker Ridge. GB – Garden Banks. KC – Keathley Canyon. Modified from Pilcher et al. (2011). (b) Schematic diagram of a gravity-driven, linked updip extensional and downdip contractional system separated by a transition zone. The updip extensional normal faulting and downdip contractional folding and thrust faulting are kinematically linked along the weak basal salt detachment. Approximate position of section line shown in (a). Modified from Applied Geodynamics Laboratory, UT-Austin. (For interpretation of the references to colour in this figure legend, the reader is referred to the Web version of this article.)

10^{-12} s^{-1} ; Jackson and Talbot, 1986) than those observed in most geologic systems (10^{-13} to 10^{-15} s^{-1} ; Pfiffner and Ramsay, 1982), salt flow can impact rate-dependent processes such as salt-sediment loading rates, sediment dewatering, and advective heat transport, thus allowing salt tectonics to substantially impact pore pressure, basin thermal evolution, and maturation processes. Despite this, many first-order components of salt evolution remain poorly understood, and as result, evolutionary models for many of these fields may vary.

Kinematic restorations are fundamental tools for testing structural interpretations in both industry and academia. However, they are often based purely on geometric line length and area balancing assumptions and rarely yield unique solutions, especially in settings that involve non-coaxial deformation and volumetric strain such as evaporite basins. Additionally, as finite deformation (and hence structural damage) is dependent not only on the final structural geometry but also the stress and strain paths (Karig and Hou, 1992), comprehensive characterization of strain damage requires an understanding of the forces driving deformation. Ideally, restorations would be carried out while keeping a strain “budget”, yet constitutive equations governing deformation mechanics cannot be run in reverse thus, it is impossible to carry out numerical tasks such as “uncreeping” salt. However, it may be possible to evaluate the viability of structural evolution models by creating forward finite element models of restoration sequences constrained within geologically realistic mechanical frameworks. If these geodynamically viable models are coupled with suitable geologic material properties, physical mechanisms such as salt inflation and diapirism and the resultant finite strain magnitudes and geometries of wall rocks may be characterized. In many Paleogene to recent basins (i.e., Atlantic passive margin systems), suprasalt sediments are presumably weak and poorly consolidated, and thus are susceptible to plastic strain and subseismic reservoir damage. In materials such as these, the finite strain history of material will influence its mechanical and hydrodynamic properties in the present day (Karig and Hou, 1992; Tang et al., 2002), and thus the ability to reconstruct these finite strain paths could have tremendous implications for testing a range of structural evolution models. Additionally, they may allow for prediction of pervasive (subseismic) structural damage that results in reduced porosity and permeability, and effectively acts to compartmentalize hydrocarbon reservoirs.

In this study, we investigate the utility of integrating kinematic restoration models with forward structural evolution (finite element) models to; (1) determine the physical viability of salt-related mechanisms such as anticline inflation and rapid salt sheet emplacement interpreted from kinematic restoration models, (2) determine the magnitude and spatial distribution of pervasive ‘subseismic’ reservoir damage accommodated by near-salt sediments during each phase of the interpreted structural evolution, and (3) examine the developmental

mechanisms of major salt structures and their influence on the temporal and spatial evolution of the stress field, with a particular emphasis on how such stress evolution may impact drilling predictions. Although hydrocarbon fields can form throughout these evaporite systems, this case study focuses exclusively on the evolution of major anticlinal traps cored by salt, similar to many downdip structures in passive margin Atlantic basins.

2. Passive margin salt basins

Although passive margin salt basins display a broad range of structural styles, most of them include an updip (landward) extensional zone dominated by listric normal faulting, rollover expulsion, and reactive diapirism, a mid-slope transition/translational zone, and a downdip (seaward) contractional zone dominated by salt-cored folds, thrust faults, active diapirism, and extrusive salt sheets and canopies (Hudec and Jackson, 2007, Fig. 1). These zones are kinematically linked through evaporite detachment horizons, where salt layers flow beneath relatively-thick overburden strata (up to 10 km thick), leading to discrete and pervasive extensional and contractional overburden deformation, diapirism, and allochthonous canopy formation. At the margin scale, salt flow is dominantly driven by gravitational loading, wherein a halostatic pressure gradient is produced due to laterally varying overburden thickness above a tabular salt layer. Resistance to flow is governed by the strength of the overlying overburden section and the magnitude of frictional boundary drag along the salt-sediment and salt-basement interfaces (Hudec and Jackson, 2007).

Three prevailing mechanism are invoked to explain diapir formation; passive, reactive, and active diapirism. Although these mechanisms are kinematically and mechanically distinct, they have been interpreted as sequential evolutionary stages of diapir formation (Hudec and Jackson, 2007). In most systems, diapirs are interpreted to result from reactive behavior, wherein extension of the suprasalt cover sequence leads to diapirism, or passive behavior, wherein the diapir remains exposed at the surface as sediment is deposited on the flanks (Jackson and Vendeville, 1994). These two mechanisms are often invoked in the extensional parts of linked salt systems, where the overall divergent horizontal stress condition can both create new diapirs through reactive behavior and then preserve such features as passive diapirs. However, the interpretation that most salt diapirs are either reactive or passive implies that salt is responding to structural evolution, rather than driving it. Additionally, it seems unlikely that either passive or reactive behavior could be reasonably invoked to explain diapir formation and salt sheet emergence in the more downdip contractional parts of the linked salt system. However, active diapirism, wherein salt actively drives overburden deformation, is also rarely invoked in traditional studies because of the commonly held perception

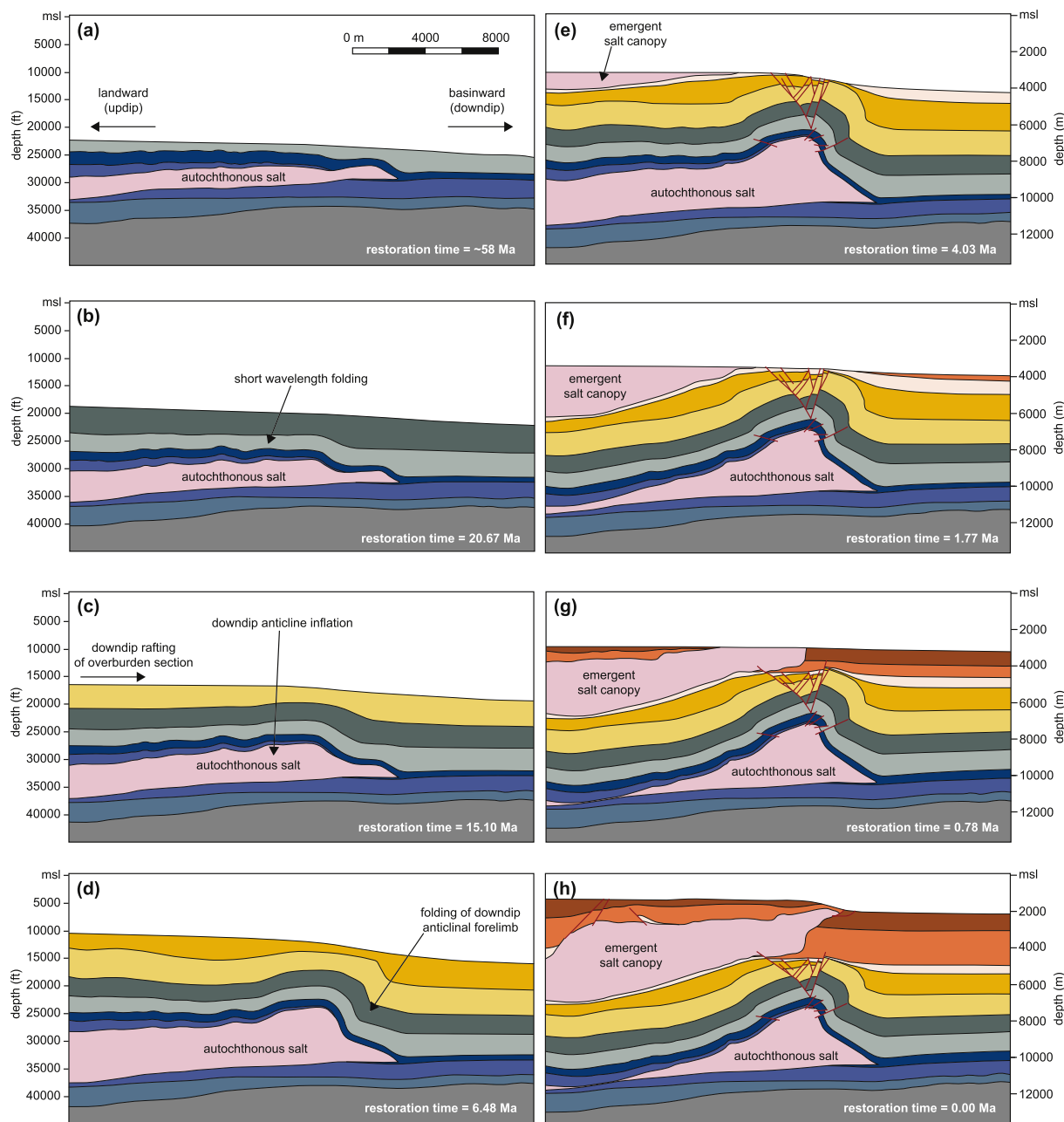


Fig. 2. Kinematic restoration model of a major anticline in the Atwater fold belt showing the major kinematic evolution phases interpreted for this structure. In the incipient phases of fold development (a–b), downdip migration of salt generates short wavelength folding and thrusting in the carbonate layer overlying salt and minor inflation of the autochthonous salt body. (c–d) As the sedimentary beam overlying salt thickens, the wavelength of contractional folding progressively increases to accommodate the continued downdip shortening, with most of the shortening budget being accommodated by folding in the forelimb of the larger anticline structure. This phase also represents a period of salt inflation that is interpreted from the kinematic restoration. (e–f) We interpret that continued salt inflation and build-up of halostatic pressure eventually drives failure of the overlying sediment beam ~20 km updip (to the left side) of the anticlinal fold, consequentially leading to expulsion of the allochthonous salt canopy and collapse of the anticlinal backlimb. Folding due to backlimb collapse drives development of the crestal graben as the top of the anticline goes into extension. (g) The rate of canopy expulsion declines as the collapsing backlimb begins to weld, thus limiting the salt supply driving canopy emplacement. (h) At present-day, a renewed cycle of sedimentary loading by minibasin development above the salt canopy drives further basinward migration of the allochthonous canopy.

that salt is too weak to deform thick overburden and wall rocks. Thus, understanding how major diapirism occurs in contractional systems, such as downdip fold belts, remains less well understood.

3. Kinematic analysis of the atwater fold belt

Even though finite element models are essentially free models (i.e., the kinematic evolution of the system is not explicitly defined), it is useful to develop broad kinematic evolution constraints to determine if

the numerical models are following a kinematically-valid structural evolution. To address this, we developed a kinematic restoration of a salt-cored anticline overlain by an allochthonous salt canopy in the Atwater belt of the Gulf of Mexico (Fig. 2) to identify the sequence and timing of major structural phases and to produce a series of reference geometries that could be compared to forward finite-element results.

For the restoration methodology applied here, it is useful to explain key techniques and assumptions, particularly as kinematic reconstructions that include major salt structures are inherently non-unique (e.g.,

Rowan, 1993). The restoration was completed using the Move software suite from Midland Valley and includes corrections for compaction, flexural isostatic effects, and thermal subsidence of the underlying crust. Unfolding is executed using the flexural slip algorithm, with layers at each time step being unfolding to a target datum interpreted to represent the bathymetric surface at each model interval. Bathymetric gradients for each interval are interpreted from the depositional stratigraphic response using the following assumptions; (1) gradients < 0.2° lead to no dynamic sediment effects, (2) gradients of 0.5–1.0° yield distributary sedimentary systems, (3) gradients of ~5° lead to sediment bypass, and (4) gradients of ~10° yield active erosion (Kneller, 1995). During intervals that include sediment erosion, particularly on the crest of the anticline, the interpreted eroded section is also restored.

One of the major challenges for kinematic restorations that involve considerable salt is that these rheologically weak bodies can flow very easily and thus deformation inherently involves non-plane strain. However, if the section chosen is oriented perpendicular to the interpreted direction of dominant salt flow and the structures resulting from such flow (i.e., normal faults, folds, salt canopies, etc.) support that interpretation, then it can be reasonably assumed that salt area (as a proxy for volume) is preserved in the section restoration, and this provides a useful constraint for restoration geometries (e.g., Hossack, 1995). Here, the primary controls on salt volume include basement dip, bathymetric gradient, bathymetric relief, and the backlimb position. Constraining salt evolution through time in these systems is critical, because the deep salt flow rate during inflation and subsequent deflation of the downdip fold representing the incipient hydrocarbon field is a fundamental component of the geologic history and thus it must be duplicated in the forward finite element model.

4. Finite-element (numerical) modeling

Over the last ~10 years, a number of salt tectonic studies (e.g. Ings et al., 2004; Gemmer et al., 2004, 2005; Gradmann et al., 2009; Allen and Beaumont, 2012) have been undertaken using finite-element techniques. These studies examined the influence of salt basin parameters such as widths and thicknesses of pre-depositional autochthonous salt, progradation rate, water loading, and overburden strength. Allen and Beaumont (2012) used finite element models to compare the compaction and bulk density scaling relationships between natural values and those inherent to analogue models. That study recognized a major change in structural architecture between natural parameters and those commonly used in analogue simulations, wherein models with natural parameters tended to develop expulsion rollover structures rather than the diapir-minibasin pairs observed in numerical simulations with physical model parameters. Perhaps most importantly, they demonstrated the potential for using finite-element techniques for testing the mechanical and thermal dynamics in these systems. For this study, we use 2-D plane strain finite-element models developed and run using the Elfen numerical codes from Rockfield Global. A more complete description of the computational framework is covered elsewhere (Peric and Crook, 2004; Thornton and Crook, 2014), and only the significant elements are discussed here.

The mechanical governing equation is that of linear-momentum balance:

$$\nabla \cdot (\sigma' + \alpha I p_f) + \rho(\phi)g = 0$$

where ∇ represents the spatial gradient, σ' is the effective stress tensor, α is the Biot coefficient, I is the second order identity tensor, p_f is the pore pressure, $\rho(\phi)$ is the porosity-dependent bulk density, and g represents the acceleration of gravity. The Biot coefficient accounts for the impact of grain compressibility on the stress change induced by a change in pore pressure. From a bulk volumetric strain perspective it is defined as:

$$\alpha = 1 - \frac{K}{K_s}$$

where K is the bulk modulus and K_s is the grain stiffness (Thornton and Crook, 2014). Note that deformation is assumed to be quasi-static and hence inertial terms are omitted from the governing equation. Spatial discretization then provides the semi-discretized finite element equations as a system of linear algebraic equations.

An explicit solution procedure is preferred for the mechanical field and a central difference time integration scheme is used to advance the solution in time. Typically, small time steps are necessary, with the critical time step for the domain dictated by the wave speed traveling through the smallest element in the mesh. The deformation of the system over geological time is assumed to occur under effectively quasi-static conditions such that the contribution from inertial forces is negligible. The Lagrangian kinematic description of the deformation can result in distortion of the finite element mesh for the magnitude of strain expected which, if left untreated, can result in poor solution quality or even termination of the solution procedure. The code manages mesh distortion by imposing an intermittent remeshing algorithm that is triggered by excessive volume change within an element group or by excessively high or low element intersection angles. For our models, we chose to use volume distortion limits of 20% to trigger remeshing, similar to that used in other forward modeling studies that employ the Elfen codes (e.g., Nikolinakou et al., 2014a,b, 2017).

5. Material properties

In most numerical models of geologic materials, rock strength is approximated using a Mohr-Coulomb constitutive property (Fig. 3a) that behaves elastically prior to reaching failure. Although this material best approximates rocks that have experienced significant diagenesis, it is likely not representative of the relatively young sediments observed overlying salt in many modern passive margin systems. In these settings, high porosity rocks composing the upper few kilometers of suprasalt overburden can experience plastic compaction, strengthening, and even pervasive cataclastic deformation via development of deformation bands (e.g., Fossen et al., 2007), all of which can accommodate substantial quantities of the total strain budget. This type of yielding is better approximated using a critical state constitutive model similar to those applied in soil mechanics (e.g. Schultz and Siddharthan, 2005). Here, the carbonate unit directly overlying the evaporite layer and the clastic sedimentary layers are modeled using the Soft Rock 3 (SR3) constitutive model developed by Rockfield Global. This modified Cam Clay critical state model (Fig. 3b–c) is a single surface rate-independent non-associated elastoplastic model (Crook et al., 2006). The primary yield function is a three-invariant surface that intersects the pressure axis in both tension and compression and is defined as:

$$\Phi(\sigma, \varepsilon_p^p) = g(\theta, p)q + (p - p_t) \tan \beta \left(\frac{p - p_c}{p_t - p_c} \right)^{1/n}$$

where p is the effective mean stress, q is the deviatoric stress, θ is the Lode angle and may be considered as a representation of the current loading/stress condition in the deviatoric plane, p_t is the tensile intercept of the yield surface with the pressure axis, p_c is the pre-consolidation pressure or compressive intercept of the yield surface with the pressure axis, β and n are material constants that define the shape of the yield surface in the p - q plane and $g(\theta, p)$ is a function that controls the shape of the yield function in the deviatoric plane (Crook et al., 2006). The specification of the constants β and n together with the initial preconsolidation pressure defines the slope of the critical state line, M , which does not evolve with deformation (Fig. 3b). The evolution of the primary yield function is governed by the void ratio or plastic volumetric strain (ε_p^p) via a piecewise linear hardening/softening law. By using fracture energy regularization, this model is able to avoid the impact of size and mesh dependence on the softening process

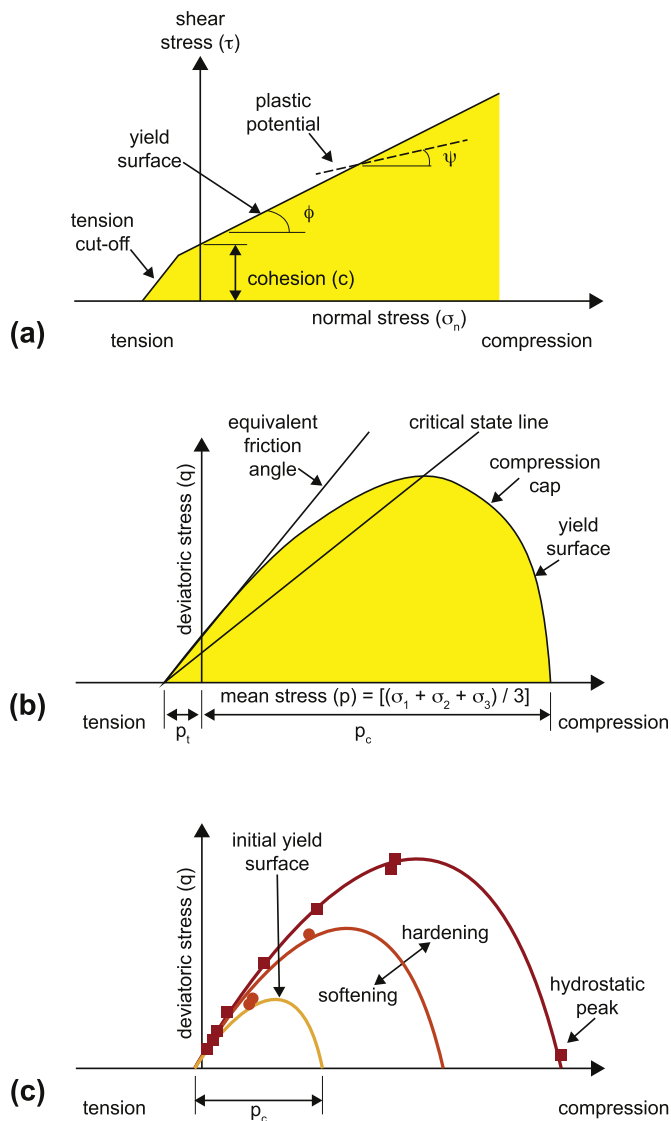


Fig. 3. (a) Mohr-Coulomb failure envelope commonly used to characterize elastic range and failure conditions for brittle-frictional geologic materials. (b) Modified critical state envelope commonly used to model poro-elastoplastic (unconsolidated) sediments, such as those in Paleogene to recent sediments in Atlantic passive margin basins. Stress conditions outside of the yield surface define the onset of plastic failure and associated material strengthening. (c) Critical state yield envelopes evolve through time as a function of porosity change. Envelopes can be defined by determination of failure conditions in triaxial tests under a range of axial and confining stresses (red squares and orange dots represent mean and deviatoric stress conditions at failure in multiple triaxial tests). p_c = initial pre-consolidation pressure. (For interpretation of the references to colour in this figure legend, the reader is referred to the Web version of this article.)

(Crook et al., 2003). Where possible, the sediments are characterized using geomechanical studies from triaxial and hydrostatic tests from equivalent Gulf of Mexico materials. Simulations were run using two different strength profiles for the overburden siltstone. The peak strength envelope for the material is defined based on specification of the various constants, particularly β and n . However, for convenience and to make the characterization more relatable, they are described in terms of the Mohr-Coulomb equivalent peak friction angle in Table 1. In this study, we ran simulations using overburden materials with two different equivalent peak friction angles. An equivalent friction angle of 32° was used to represent a relatively strong material with no pore fluid overpressure for simulations CM1 and BC1 and was derived from

Table 1

Mechanical properties for overburden sediment, suprasalt carbonate, and salt model materials. For overburden siltstone, sandstone, and carbonate density values represent initial depositional conditions; parameters evolve during burial/deformation and associated plastic compaction.

Overburden siltstone	
Youngs modulus (E)	Nonlinear stress and porosity dependent
Poisson's ratio (ν)	0.3
Initial bulk density (ρ)	1968 kg m^{-3}
Equivalent friction angle (ϕ - CM1 and BC1)	32°
Equivalent friction angle (ϕ - RS2)	18°
Initial porosity	0.50
Initial preconsolidation pressure	1.5 MPa
Overburden sandstone	
Youngs modulus (E)	Nonlinear stress and porosity dependent
Poisson's ratio (ν)	0.25
Density (ρ)	2075 kg m^{-3}
Friction angle (ϕ)	35°
Initial porosity	0.45
Initial preconsolidation pressure	2.0 MPa
Suprasalt carbonate	
Youngs modulus (E)	Nonlinear stress and porosity dependent
Poisson's ratio (ν)	0.20
Density (ρ)	2365 kg m^{-3}
Equivalent friction angle (ϕ)	41°
Initial porosity	0.30
Initial preconsolidation pressure	15.0 MPa
Salt	
<i>Elastic</i>	
Youngs modulus (E)	31,000 MPa
Poisson's ratio (ν)	0.35
Density (ρ)	2200 kg m^{-3}
Friction angle (ϕ)	0.01
<i>Viscoplastic</i>	
A_1	$5.95 \text{ e}22 \text{ s}^{-1}$
A_2	$6.87 \text{ e}12 \text{ s}^{-1}$
Q_1	25,000
Q_2	10,000
n_1	5.5
n_2	5.0
Shear modulus (μ)	12400
Universal gas constant (R)	1.987

numerical studies within the Gulf of Mexico (e.g., Nikolinakou et al., 2017). Based on the results of those initial models runs, we ran a final simulation (RS2) with an overburden equivalent peak friction angle of 18° to approximate rheological weakening due to overpressure development (e.g., Casey et al., 2016), which is common in the Gulf of Mexico. Although the yield envelopes tend to increase in size as deformation and compaction continue, the equivalent peak friction angle remains constant (Fig. 3c).

In natural systems, overburden bulk density and material strength constantly evolve as a function of average porosity, which is in turn a function of how stress state, dewatering state, and local and regional permeability control burial compaction. In such a system, the bulk density is constantly evolving throughout the burial history, and thus buoyancy forces themselves are transient and cannot be reasonably approximated with fixed values. The critical state framework implicitly accounts for volumetric changes, and by extension changes in sediment bulk density, not only due to burial compaction or localized shear (strain hardening and softening, respectively) but also due to salt inflation and lateral compression as the fold belt develops. The above implies that with an effective stress solution for stress state, excess pore pressure can inhibit primary consolidation and therefore influence salt deformation drivers such as density inversion. Although the models presented here do not accommodate explicit coupling of pore pressure and geomechanical fields, the computational framework does support such coupling (e.g., Nikolinakou et al., 2017) and will thus be a target for a future study. Another assumption is that bulk density evolution is

governed solely by changes in effective stress and thus material state evolution is not influenced by thermally-driven diagenetic processes. Although this is also possible in the current numerical framework, much of the overburden in the Gulf of Mexico is comparatively young and so we interpret the influence of diagenesis here to be relatively minor.

Salt is modeled using a modified steady-state form of the Munson-Dawson multi-deformation mechanism constitutive law (Munson and Dawson, 1982, 1984). In this model, the steady-state creep strain rate $\dot{\epsilon}_c$ is defined as:

$$\dot{\epsilon}_c = A_1 \left(\frac{\bar{\sigma}}{\mu} \right)^{n_1} e^{-Q_1/RT} + A_2 \left(\frac{\bar{\sigma}}{\mu} \right)^{n_2} e^{-Q_2/RT}$$

where A_1 , n_1 , A_2 , and n_2 are material constants for creep components, $\bar{\sigma}$ is the steady-state effective stress, μ is the bulk modulus, Q_1 and Q_2 are the activation energies for creep components, R is the universal gas constant, and T is the absolute temperature. The value of μ is temperature-dependent and is defined as:

$$\mu = \mu_o - \frac{d\mu}{dT} (T - T_o)$$

where T_o is the temperature at which the reference bulk modulus μ_o is measured. The model as presented accounts for steady state creep due to dislocation climb and an experimentally defined but mechanically uncharacterized mechanism. It is assumed that deviatoric stresses over geological time do not reach sufficient magnitudes for dislocation glide to be significant. The characterization of Gulf of Mexico salt (Fredrich et al., 2003) indicates that dislocation glide is important when deviatoric stress is in excess of 20.5 MPa. Whilst such stress changes may be expected during production related activities (e.g., depletion induced stress changes), deviatoric stress changes over geological timescales are expected to be more subtle. Likewise, transient creep is not judged to be important over these timescales. Constitutive parameters reflect Avery Island salt (Table 1), which is dominated by a halite mineralogy, similar to many other coastal domal salt bodies (Fredrich et al., 2007). Finally, because we are not considering internal deformation of the crustal basement units beneath the initial autochthonous salt layer, the continental, transitional, and oceanic crust is modeled using variations of a simple drained poroelastic model (Table 2).

6. Experimental design and boundary conditions

In this study, finite-element modeling was carried out in three phases. All three variants of the model included the same basic geometry and boundary condition setup of a weak salt horizon overlain by carbonate that this is progressively loaded by a basin prograding sedimentary wedge (Fig. 4). The first phase of modeling involved development of a simplified prototype margin model (CM1) followed by a full margin scale base case model (BC1) and a final model that includes significantly reduced overburden sediment strength (RS2). In these

systems, the prograding wedge represents sedimentation occurring in the Gulf of Mexico from late Cretaceous to present, including the associated seaward migration of the shelf edge. In the models, depositional intervals are specified by directing the model to allow accumulation of depositional fill between the current model surface and a datum defined for each interval. For segments of the predefined datum that have a lower elevation than the model surface at a given time step, deposition will not occur. Although the evolution of the model bathymetry through time influences deposition rates, the timing of depositional intervals and the datum positions are adjusted to generate average regional deposition rates that are similar to those observed from wells in the Gulf of Mexico system (1–2 mm yr⁻¹; Galloway et al., 2000). In parts of the model that develop minibasins due to salt withdrawal, local deposition rates may be substantially higher (> 5 mm yr⁻¹; Peel et al., 1995; Galloway, 2008).

In the conceptual CM1 model, the base of the model was fixed and did not include an isostatic response to sedimentary loading. Because the magnitude of inflation of the downdip fold is primarily a result of the halostatic ‘head’ of the underlying autochthonous salt, modification of the slope beneath this salt body should influence the pressure magnitude at the salt-sediment interface. To address this, the base case model (BC1) and the reduced strength variant (RS2) employ a scheme to calculate the isostatic response. Because the overall isostatic balance must consider the weight of the overlying sediment matrix and the water column from sea level, we utilized a combined approach of opposing forces (Supplementary Fig. 1). At the base of the crust, we applied an upwards-directed hydrostatic face load equivalent to the buoyancy force generated by the underlying mantle fluid. To represent the overlying water column, this mantle face load is opposed by a hydrostatic gradient:

$$F = h\rho_w g$$

where the opposing force (F) is the equivalent height of the water column below sea level (h), the water density (ρ_w), and gravitational acceleration (g). This downward-directed hydrostatic force represents the weight of the overlying water column and is in addition to the force generated by the lithostatic load under gravity. In these models, a total stress analysis is employed, which ignores the strength influence of any pore fluid phase and thus the bulk density becomes the buoyant density. For the oceanic and continental crust, the flexural stiffness component is intrinsically included as a function of crustal geometry, thickness, and constitutive properties. Crustal thicknesses used in the models were derived from regional seismic reflection lines of Christeson et al. (2014). This methodology for implementing isostasy shows excellent agreement between calculated and simulated subsidence values (Supplementary Fig. 2).

A second key boundary condition is the presence of an iteratively calculated thermal field coupled to displacement and density of the mechanical field that can account for transient heat advection due to salt flow. At temperatures normally observed in sedimentary basins (0–150 °C), salt behaves as a viscous fluid under ‘normal’ geologic strain rates (10⁻¹² to 10⁻¹⁴ s⁻¹), deforming dominantly by dislocation creep in coarse-grained salt (Carter and Hansen, 1983; Wawersik and Zeuch, 1986) and diffusional (pressure-solution) creep in finer-grained salt (Urai et al., 1986; Spiers et al., 1986, Spiers and Carter, 1998; van Keken et al., 1993). In these systems, the effective viscosity (η) of salt ranges between 10¹⁷ to 10²⁰ Pa · s, mostly as a function of grain size and temperature (van Keken et al., 1993). In previous analogue and numerical models, the fixed values of viscosity (usually $\eta = 10^{18}$ Pa · s) are considered to be most appropriate for fine-grained salt at relatively high temperature (> 160 °C; van Keken et al., 1993; Allen and Beaumont, 2012). Using a two-mechanism creep law, van Keken et al. (1993) determined that regardless of grain size, a temperature decrease from 160 °C to 20 °C would result in a 1.0–1.5 order of magnitude change in salt viscosity (Supplementary Fig. 3). Because temperature changes of this magnitude are likely to be observed in most sedimentary

Table 2

Mechanical properties for continental and oceanic crust at the base of models BC1 and RS2. All crustal basement units modeled as simple elastic materials with a high stiffness and negligible porosity. Although oceanic crust is generally denser than continental crust, both materials were assigned the same bulk density to prevent complications during establishment of isostatic equilibrium.

Continental and transitional (thinned) crust	
Youngs modulus (E)	70 GPa
Poisson's ratio (ν)	0.25
Initial bulk density (ρ)	2860 kg m ⁻³
Oceanic crust	
Youngs modulus (E)	70 GPa
Poisson's ratio (ν)	0.25
Density (ρ)	2860 kg m ⁻³

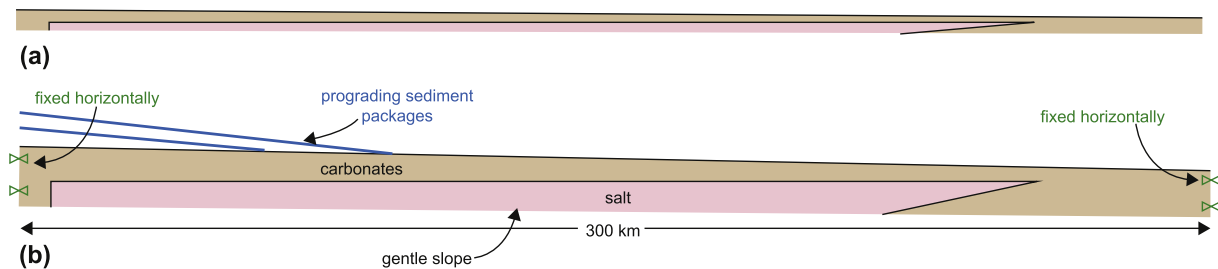


Fig. 4. Model design and boundary conditions for the conceptual (CM1) finite-element model. A similar scenario of a prograding sediment wedge deposited on a carbonate layer overlying an autochthonous salt body was employed for margin scale models BC1 and RS1. (a) Initial stage of CM1 model with no vertical exaggeration and (b) 3:1 vertical exaggeration to highlight model components.

basins, salt viscosity should be highly variable.

To address this, the models BC1 and RS2 include a temperature field that is coupled to the mechanical field at discrete time steps. The salt material model is a modified temperature-dependent multi-mechanism creep model (Munson and Dawson, 1982, 1984; Fossum and Fredrich, 2002). The temperature field, which will consider conduction, radiogenic heat production, heat advection, and a basal mantle heat flux, is calculated separately and then is coupled to the mechanical field, which in turn calculates salt creep rate. Heat flow in porous media saturated with a single fluid phase is derived from the conservation of energy and is expressed as the advective-diffusion equation:

$$(\rho c)_b \frac{\partial T}{\partial t} = \text{div}(\kappa_b \nabla T) + (\rho_f c_f q_f \cdot \nabla T) + Q_b$$

where subscripts *b*, *f*, and *s* denote bulk, fluid, and solid grain values and κ is the thermal conductivity, *T* is temperature, Q_b is the radiogenic heat production, ρ is the bulk density, *c* is the specific heat, and q_f is the Darcy fluid flux. Volumetric heat generation resulting from radioactive decay of uranium (U), thorium (Th), and potassium (K) is defined as:

$$Q_r = 0.01\rho_b(0.52U + 2.56Th + 3.48K)$$

by Hanstchel and Kauerauf (2009). U and Th concentrations are defined in ppm and K concentration is defined in weight percent. Given that explicit consideration of fluid flow is not considered, the primary heat transfer is that of conduction. This assumption is generally appropriate except where formations are highly porous or intensely fractured. Thermal properties for each material are shown in Table 3. The governing equation for heat flow is solved implicitly because of the relaxed constraints on time step size.

7. Results

7.1. Kinematic restoration model

In the Atwater fold belt, the downdip contractional fold for this case study is interpreted to evolve through multiple stages, including: (1) early short-wavelength (1.5–3.0 km) folding/thrusting of the carbonate and sediments overlying the autochthonous salt as seaward directed salt flow initiates (Fig. 2a–b), (2) progressive inflation of the downdip parts of the autochthonous salt and associated folding of the downdip anticline forelimb (Fig. 2c–d), (3) initial collapse of the fold backlimb as the sediment beam overlying salt is breached updip of the major contractional folds, followed by development of the crestal graben due to fold bending (Fig. 2e), (4) accelerating backlimb collapse and extrusion of a major salt canopy (Fig. 2f), and (5) basal welding of the collapsed backlimb and associated reduction in salt flow rates into the emerging allochthonous salt canopy (Fig. 2g–h). During this evolution, salt inflation continued despite the deposition of > 4 km of overburden sediment. Although not documented in our restoration, the initial collapse is interpreted to result from active or reactive diapiric breaching of this thick sediment beam updip of the fold due to elevated halostatic pressure generated by the basin prograding sedimentary wedge. As will

Table 3

Thermal properties for all material units. Thermal properties for continental, transitional, and oceanic crust include representative heat-production of granitic, serpentinized peridotite (cooled upper mantle), and basalt, respectively. Bulk density values represent initial values and evolve during burial.

Model thermal boundary conditions	
Ambient surface temperature	25 °C
Basal mantle heat flux	0.050 W m ⁻²
Overburden siltstone	
Thermal conductivity (<i>k</i>)	2.05 W m ⁻¹ K ⁻¹
Thermal diffusivity (κ)	1.55 × 10 ⁻⁶ m ² s ⁻¹
Internal heat generation (<i>A</i>)	0.50 μW m ⁻³
Specific heat capacity (<i>c</i>)	911 J kg ⁻¹ °C ⁻¹
Overburden sandstone	
Thermal conductivity (<i>k</i>)	3.95 W m ⁻¹ K ⁻¹
Thermal diffusivity (κ)	3.19 × 10 ⁻⁶ m ² s ⁻¹
Internal heat generation (<i>A</i>)	0.66 μW m ⁻³
Specific heat capacity (<i>c</i>)	854 J kg ⁻¹ °C ⁻¹
Suprasalt carbonate	
Thermal conductivity (<i>k</i>)	2.90 W m ⁻¹ K ⁻¹
Thermal diffusivity (κ)	2.36 × 10 ⁻⁶ m ² s ⁻¹
Internal heat generation (<i>A</i>)	0.12 μW m ⁻³
Specific heat capacity (<i>c</i>)	848 J kg ⁻¹ °C ⁻¹
Salt	
Thermal conductivity (<i>k</i>)	6.50 W m ⁻¹ K ⁻¹
Thermal diffusivity (κ)	3.43 × 10 ⁻⁶ m ² s ⁻¹
Internal heat generation (<i>A</i>)	0.00 μW m ⁻³
Specific heat capacity (<i>c</i>)	860 J kg ⁻¹ °C ⁻¹
Continental crust	
Thermal conductivity (<i>k</i>)	3.0 W m ⁻¹ K ⁻¹
Thermal diffusivity (κ)	1.32 × 10 ⁻⁶ m ² s ⁻¹
Internal heat generation (<i>A</i>)	1.59 μW m ⁻³
Specific heat capacity (<i>c</i>)	790 J kg ⁻¹ °C ⁻¹
Transitional crust	
Thermal conductivity (<i>k</i>)	3.0 W m ⁻¹ K ⁻¹
Thermal diffusivity (κ)	1.32 × 10 ⁻⁶ m ² s ⁻¹
Internal heat generation (<i>A</i>)	0.17 μW m ⁻³
Specific heat capacity (<i>c</i>)	790 J kg ⁻¹ °C ⁻¹
Oceanic crust	
Thermal conductivity (<i>k</i>)	3.0 W m ⁻¹ K ⁻¹
Thermal diffusivity (κ)	1.32 × 10 ⁻⁶ m ² s ⁻¹
Internal heat generation (<i>A</i>)	0.17 μW m ⁻³
Specific heat capacity (<i>c</i>)	790 J kg ⁻¹ °C ⁻¹

be discussed in detail later, such a scenario is key to understanding the evolution of these folds underlying major salt canopies.

7.2. Conceptual model (CM1)

In the first phase of modeling, the weak halite substrate responds to progressive loading by a basin-prograding sedimentary wedge by flowing basinward (downdip; Fig. 5a). This leads to the mobilization of the autochthonous salt layer in the basinward direction. On the continental (left) end of the section, salt mobilization leads to extension of the overburden cover sequence and in turn to the development of reactive diapirs that rise through the extended overburden (Fig. 5b).

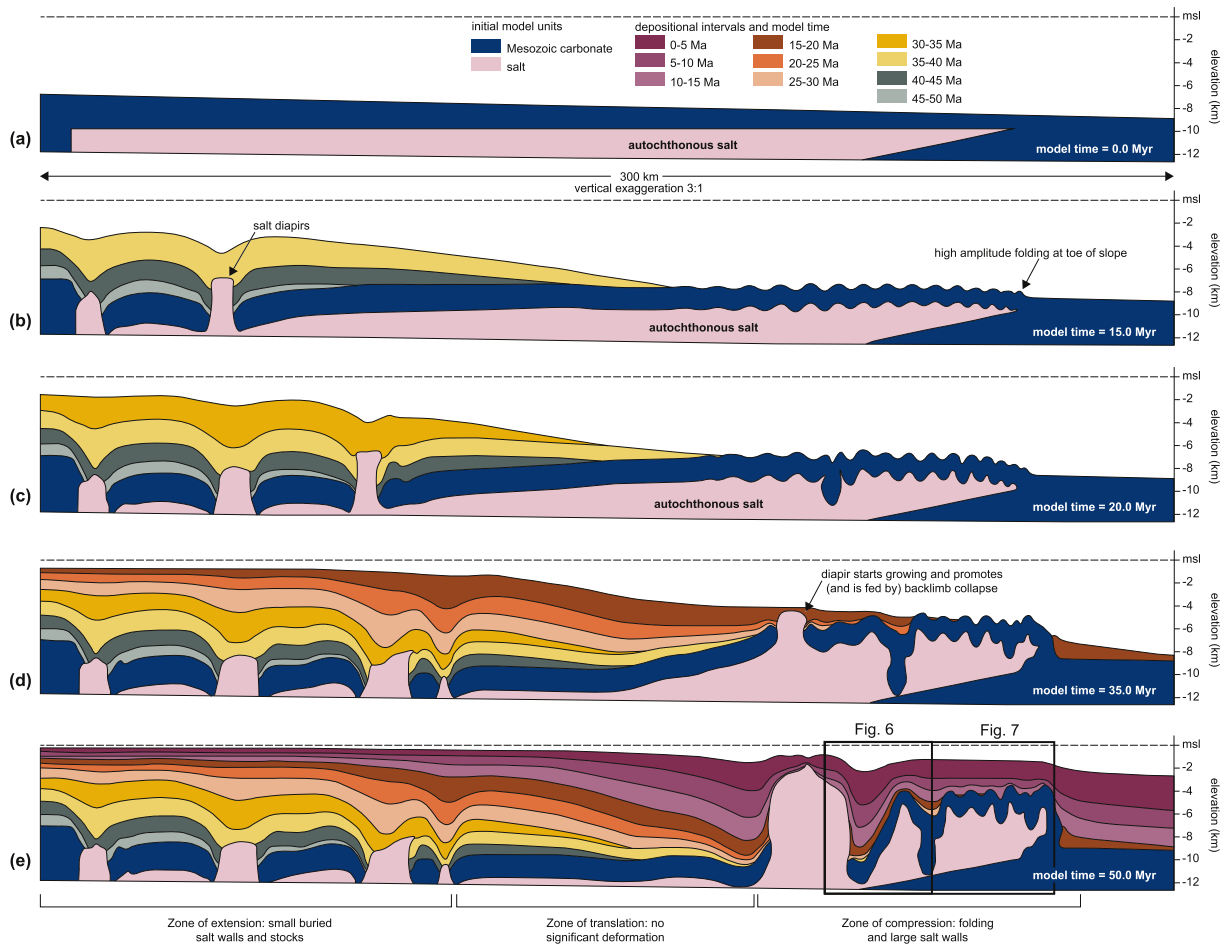


Fig. 5. Results from the simplified conceptual finite element model (CM1). (a) Initial model geometry includes a ~2.5 km thick autochthonous salt layer overlain by a carbonate material representing the Mesozoic carbonate section in the Gulf of Mexico. (b) At a model time of 15 Myr, early basinward progradation of the sediment wedge drives basinward salt flow and short wavelength, high amplitude folding of the carbonate layer, which is rafted above the salt flow. (c) As folding continues at a model time of 20 Myr, foundering of part of the carbonate beam begins to compartmentalize the downdip autochthonous salt into two distinct zones. (d) Following welding of the foundered segment of the carbonate section at a model time of ~40 Myr, a nascent diapir begins to form updip of the weld point. Formation of this diapir acts as a pressure release valve, allowing rapid collapse of both the backlimb downdip of the diapir and the overburden sequence updip of the diapir. The collapse of both of these features drives rapid salt flow into the major diapir region, (e) which ultimately stabilizes at ~50 Myr model time as a result of welding of the updip overburden sequence and near-welding of the collapsed backlimb downdip of the salt diapir. In this model, sedimentation rates were sufficiently high to prevent the emergence of the salt feeder as a major allochthonous salt canopy.

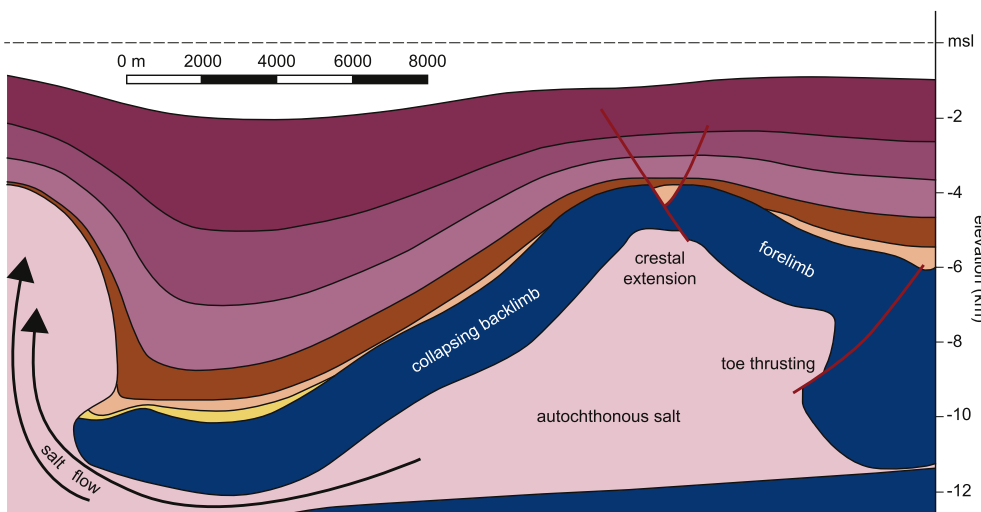


Fig. 6. Zoomed segment of CM1 model results (location shown on Fig. 5) that highlight some components of the model that are consistent with our interpreted evolution of the fold from the kinematic analysis. Here, onset of diapirism updip of the anticline drives rapid salt evacuation from beneath the fold backlimb, causing it to collapse and cause crestal extension at the top of the fold. In this model, the diapir did not progress to an emergent salt sheet, likely because sedimentation rates were high enough to prevent such an emergence. Faults (red) were drawn over segments of the model that developed “shear zones” that approximate faulting in continuum models such as these. (For interpretation of the references to colour in this figure legend, the reader is referred to the Web version of this article.)

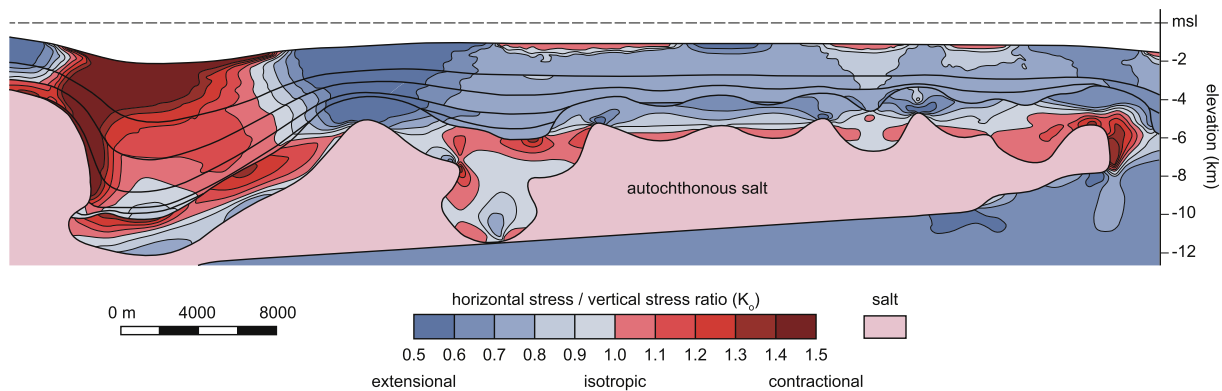


Fig. 7. K (horizontal/vertical stress ratio) results for the CM1 model at a time of 50 Myr. Following collapse of the backlimb and growth of the major diapir, the anticlines yield two clearly distinct stress fields; broadly extensional stress fields over the anticlines results in the development of normal faulting and formation of crestal grabens, whereas the backlimb adjacent to the diapir is dominated by a strongly compressional stress regime.

Vertical salt flow is driven by the progressive increase in halostatic pressure during burial of the autochthonous salt toward the updip end of the section. Salt flow toward the downdip end of the model also leads to short wavelength folding of the overburden to accommodate the updip extension (Fig. 5b). Such folding continues throughout the model evolution, albeit with an increasing fold wavelength as the sediment ‘beam’ thickens. Salt migration in the downdip direction also leads to progressive inflation of the autochthonous salt layer (Fig. 5c), with the wavelength of the inflated zones localizing within two predominant anticlines that nucleated during earlier folding. Continued inflation eventually leads to the onset of either active or reactive diapirism at the crest of the more updip inflating anticline (Fig. 5d), flow of pressurized salt toward the surface, and eventually collapse of the backlimb of the major downdip fold due to salt evacuation (Figs. 5e and 6). Expulsion continues at high rates until the collapsing backlimb reaches a welding point at the base of the autochthonous salt (Fig. 6), essentially cutting off the salt flow feeding the emergent diapir. Once the model runs to completion, the linked extensional, translational, and contractional zones above the weak mobilized layer are clearly distinguished. At the final stage of the model in the region containing the major anticline, the crest of the anticlinal structure and the zone surrounding the collapsed backlimb adjacent to the extruding salt show the greatest range of K values (0.7–1.5 depending on structural position) recorded in the model domain (Fig. 7). Relatively high K values (> 1.4) are present at the toe of the autochthonous salt. Although a region of reduced horizontal stress is predicted in the hinge of the anticline, discrete faults comprising the crestal graben noted in the restoration (Fig. 2e–h) are poorly realized. It is possible that increasing mesh resolution may permit these discrete structures to emerge in model results.

7.3. Base case model (BC1)

As a reminder, the CM1 and BC1 models differ in that the BC1 model includes a flexural isostatic response and an implicitly modeled thermal field. The thermal field is coupled to the mechanical field to allow the temperature-dependence of the salt to respond to transient changes in temperature due to heat advection during salt flow. In the BC1 model, the updip segment of the margin (to the left) evolves similar to the CM1 model, with loading by the prograding wedge driving salt flow downdip into the contractional toe (to the right; Fig. 8). In this updip region, salt flow drives overburden extension via rafting, with localized extension resulting in the development of reactive to passive (?) diapirism. In the downdip contractional segment of the system, salt flow accompanied by the establishment of a lateral gradient in lithostatic stress drives inflation of two anticlinal structures separated by a partially collapsed syncline. Unlike the CM1 model, the overburden in the contractional zone never fails but rather is continuously uplifted by

salt inflation. Because the overburden is relatively strong (equivalent friction angle = 32°) and does not extend in the contractional segment of the system, diapirism and subsequent salt sheet expulsion is unable to occur, which is incompatible with the kinematic evolution interpreted from the present-day structural geometry.

In the final stage of the model, the stress geometry and the distribution of K reflects the relative simplicity of the structure (Fig. 9). Above the two inflating salt pillows, K values < 1 indicate that the inflation driving folding is also driving outer arc extension of the anticlinal folds. In the common syncline between the two inflating anticlines, K values are higher (up to 1.1), indicating a progressively increasing contractional stress regime from the crest of the anticline to the synclinal trough. At the downdip tip of the autochthonous salt body, a zone of very high contractional K values (> 1.4) is present.

7.4. Reduced strength model (RS2)

In the Atwater fold belt, the large allochthonous salt canopy is interpreted to represent a key kinematic and stress/strain evolution feature. In the BC1 model, the strength of the overburden material limited any development of such a feature, leading us to run a second simulation with a greatly reduced strength of the overburden material. This was accomplished by reducing the critical state friction angle from 32° in BC1– 18° in RS2. The selection of the original value is justified based on other numerical studies within the Gulf of Mexico (Nikolinakou et al., 2017), whilst the reduced strength value was determined based on recent experimental testing of Casey et al. (2016).

In the RS2 model, the early evolution is similar to both the CM1 and BC1 models, with downdip migration of the salt driven by seaward progradation of the sedimentary wedge (Fig. 10). Also, as in the previous models, such salt flow leads to inflation of two major anticlinal structures. Following this inflation, the RS2 model then diverges from the behavior of the BC1 model, as rising halostatic pressure begins to drive deformation of the most seaward anticline (Fig. 11a). In the crest of that seaward anticline, salt begins actively tunneling through the ~ 4 km thick roof sequence, first as a tapered diapir but later as a ~ 2 km-wide stock that reaches the surface (Fig. 11b). Once at the surface, the release of halostatic pressure results in rapid salt sheet emplacement in the updip direction (Fig. 11c). This rapid loading by the salt sheet coupled with removal of autochthonous salt from below leads to subsequent collapse and clockwise rotation of the common limb between the two major anticline structures (Fig. 11d). This motion generates extensional faulting in the crest of the updip anticline followed by reactive and eventually active diapirism at the top of that structure (Fig. 11e). The combined effects of the salt diapir breaching the surface along with basal welding of the syncline results in stabilization of the system as the downdip salt source is cut off (Fig. 11f).

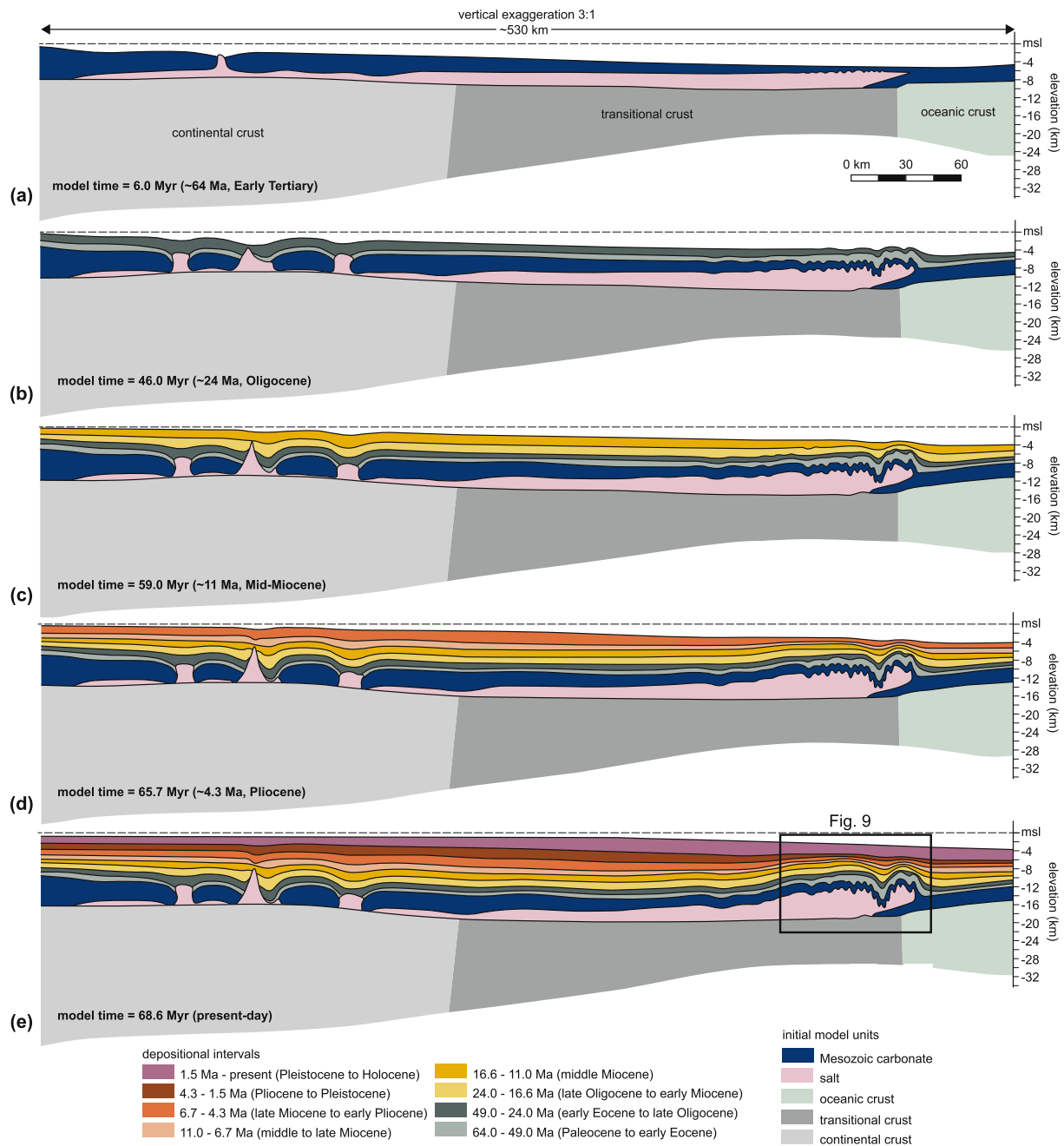


Fig. 8. Full margin-scale finite element model results for the BC1 model. An identical initial configuration and sedimentation pattern was utilized in the RS2 model, with the only difference being a substantially reduced overburden strength in the RS2 model. (a) The variable thickness of the carbonate beam has begun to drive downdip salt flow by a model time of 6.0 Myr. This flow results in extension of the updip cover sequence, subsequent localization of diapirism, and rafting of the carbonate beam to produce short wavelength folding at the downdip end of the beam. (b–d) With continued sedimentation, the sediment beam thickens, causing a subsequent increase in fold wavelength. (c) By the model time of ~59.0 Myr, this fold wavelength increase produces two major anticlines at the downdip extent of the system. (e) At the final model stage at 68.6 Myr, the strength of the elastoplastic overburden sediments (friction angle = 32°) has prevented the emergence of any diapirs in the contractional segment of the system. For the RS2 model (friction angle = 18°), most of the system yields a similar evolution with the exception of the behavior of the downdip anticlines shown in Figs. 10 and 11 (inset box). Zoomed results from the BC1 model are shown in Fig. 9.

The stress evolution of the RS2 model, like the structural evolution, proceeds through a number of distinct stages. Prior to the onset of diapirism in the downdip anticline, the K distribution is very similar to that of the BC1 model, with broadly extensional K values (i.e. < 1.0) focused over the outer arc crests of the major anticlines and contractional K values (i.e. > 1.0) focused in both the common syncline between the two major anticlines and at the downdip toe of the autochthonous salt body. With the onset of active diapirism in the crest of the most downdip anticline, K values rise rapidly in the sediment

adjacent to the diapir stock as a consequence of the horizontal forces imparted by the actively tunneling salt (Fig. 12a). When the diapir reaches the surface and the downdip halostatic pressure is released, the very high K values decrease. The release of the halostatic pressure also leads to emplacement of a large salt canopy above the common syncline between the anticlines, which drives foundering and clockwise rotation of the synclinal minibasin. This in turn drives the crest of the updip anticline into extension (Fig. 12b), which includes the development of normal faults. This extension invokes initial reactive diapirism as

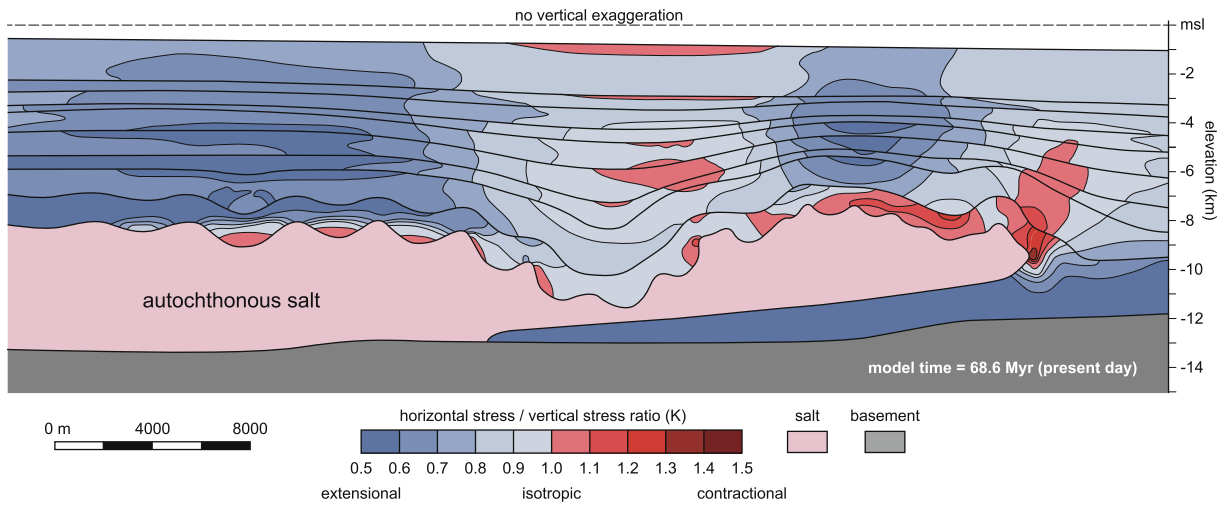


Fig. 9. K (horizontal/vertical stress ratio) condition for the BC1 model at the final stage (model time = 68.6 Myr). Although a clear extensional stress regime developed across the crest of the anticline, the frictional strength of the overburden was too great to allow failure to occur.

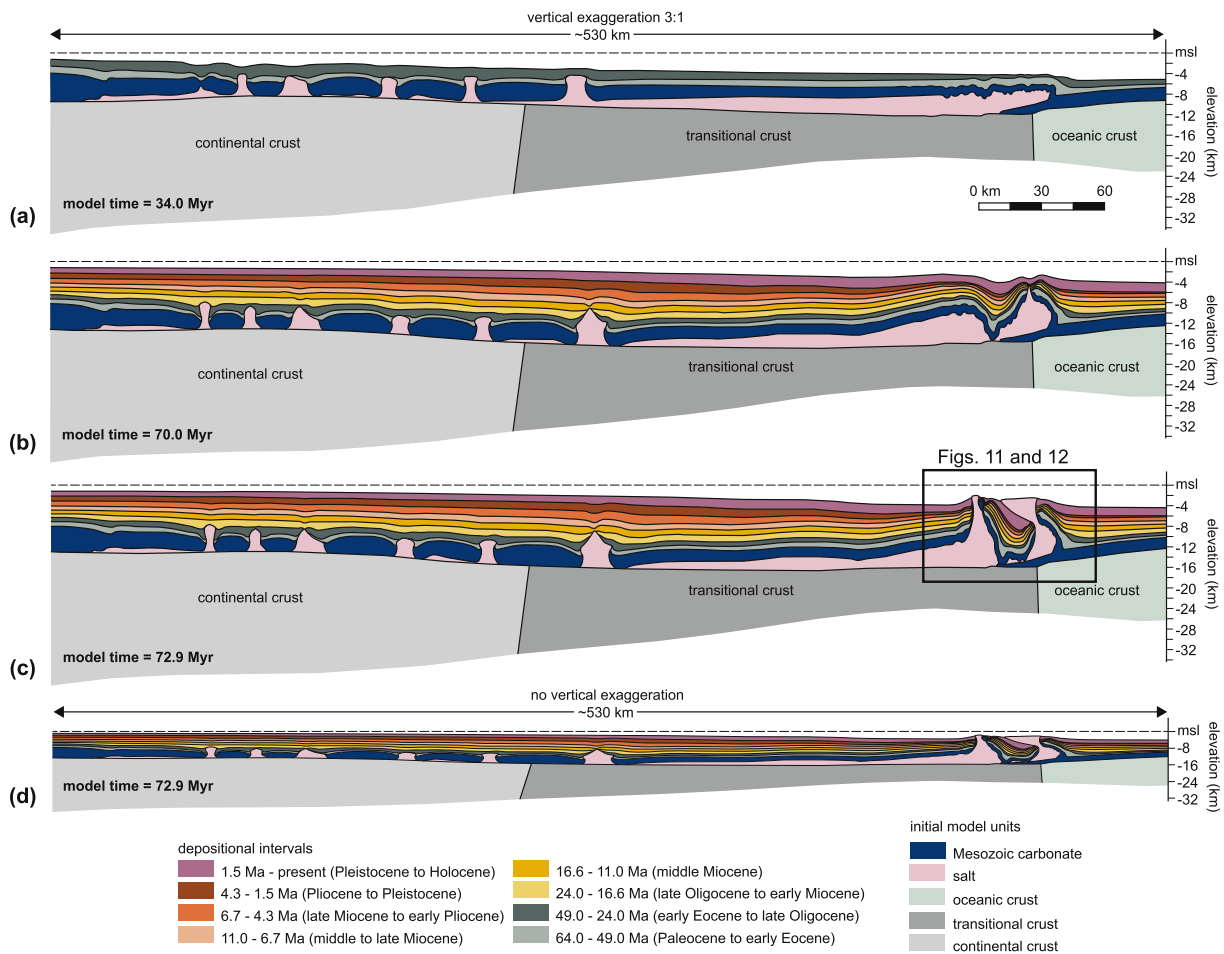


Fig. 10. Full margin-scale finite element model results for the RS2 model. An identical initial configuration and sedimentation pattern was utilized in the BC1 model. (a) Like in the BC1 model, the lateral gradient in overburden stress created by the variable thickness of the prograding sediment wedge overlying salt drives basinward (to the right) migration of the salt. At ~34.0 Myr, this flow causes rafting of the overburden sequence, which generates extensional (reactive) diapirism and short-wavelength contractional folding of the overburden sequence at the downdip toe of the system. (b) At 70.0 Myr, continued loading of the system and inflation of the downdip anticlines eventually drives the overburden system to fail above the most basinward anticline and a nascent diapir begins to emerge. (c) At 72.9 Myr, the system has stabilized after development of two diapirs and an allochthonous salt canopy in the contractional part of the system. Both diapirs localized at the crest of the major anticlines in this part of the system. (d) Same section as (c) shown with no vertical exaggeration.

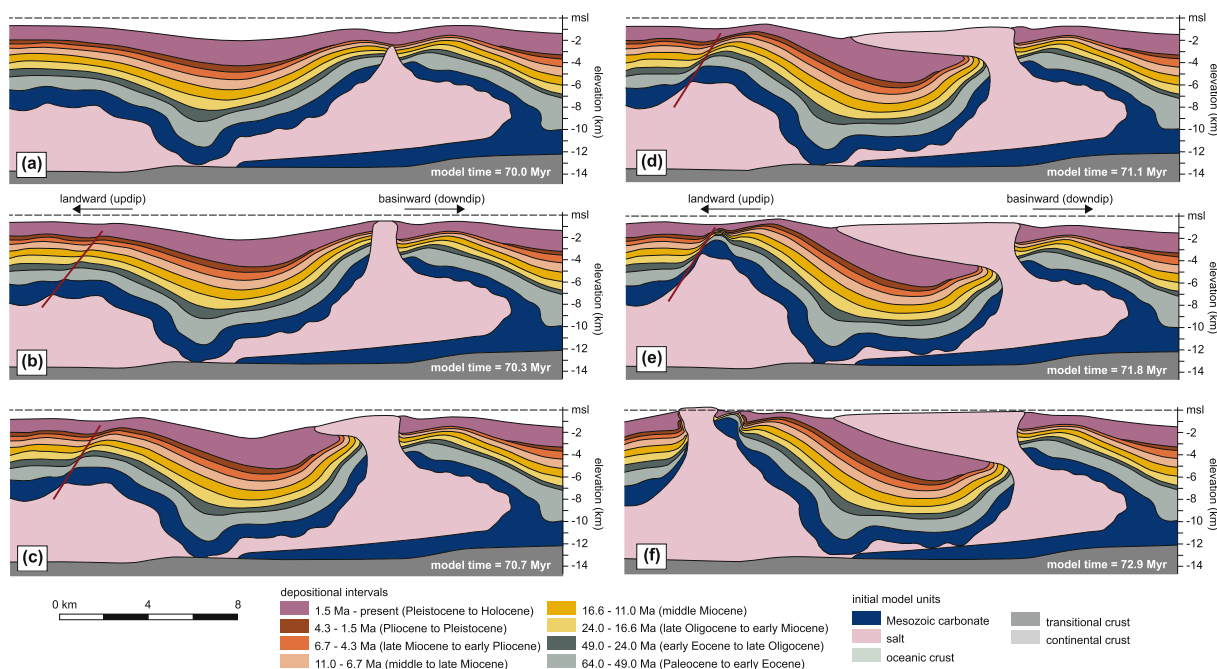


Fig. 11. Structural evolution of the contractional fold segment in the RS2 model. (a) At 70.0 Myr model time, the diapirism initiates in the downdip anticline as the cover sequence extends and thins. (b) The downdip diapir becomes emergent at a model time of ~70.3 Myr, leading to the onset of clockwise rotation of the common limb between the two anticlines. This motion also initiates a zone of normal faulting at the crest of the updip diapir. (c) Continued clockwise rotation of the common limb at a model time of 70.7 Myr drives salt evacuation toward the feeder stock while simultaneously being loaded from above by the emerging allochthonous canopy. Additionally, the salt stock and sheet drive substantial deformation (folding and plastic strain) of the overburden sediments adjacent to salt. (d–e) The salt sheet continues to emerge and thicken as the common limb founders. Simultaneously, a second diapir begins to emerge in the updip anticline, as the overburden there continues to extend along the normal fault that initiated when the common limb began rotating. In the downdip anticline, salt sheet emergence stops when the common limb reaches the basal welding point, essentially cutting off the salt flow feeding the diapir. (f) Once the downdip anticline is cut off from the updip flow of salt at ~72.9 Myr, the updip diapir continues to grow as it becomes the ‘release valve’ for the pressure generated by the prograding wedge.

halostatic pressure drives salt at the anticlinal crest to fill the void created by crestral extension. Following initial reactive diapirism, a switch occurs to active diapirism as the salt begins actively tunneling through the final ~2 km of overburden. This active tunneling leads to relatively high K values in the sediments adjacent to the rising stock (Fig. 12c), similar to the evolution of the downdip salt stock.

8. Discussion

8.1. Comparison of model results with kinematic restorations

In the earliest phases of the kinematic restoration model (58–15 Ma; Fig. 2a–c), the contractional component of the system is interpreted to experience dominantly short wavelength (< 2 km) folding (Fig. 2a–c), consistent with observations from seismic reflection profiles of the carbonate units overlying salt (Rowan et al., 2003). In the finite element models, a very similar style of folding is observed, and is presumed to accommodate shortening produced by updip rafting and extension of the salt cover sequence (Figs. 5b and 8b). With continued sedimentation in both the kinematic and numerical models, the overburden ‘beam’ thickens, leading to a progressive increase in the wavelength of contractional folding. At this stage in the kinematic model, the observation of a broadly thickened forelimb (downdip limb) is interpreted to result from an updip reduction in accommodation space produced by inflation of the allochthonous salt beneath the anticlinal crest and the backlimb (Fig. 2a–d). In the BC1 and RS2 numerical models, a similar evolution is observed, as two nascent anticlines localize the inflationary zones. Salt inflation and anticline growth are complimentary positive feedback mechanisms. In the kinematic restoration, only one such anticline is shown, but cross sections covering longer strike-perpendicular lengths from other segments of the Atwater fold belt show multiple anticlines (e.g., Rowan et al., 2003) with similar

wavelength (8–10 km) and amplitude (3–4 km) to those shown both in the kinematic restoration and in the BC1 and RS2 models. This relatively simple style of detachment folding, which often occurs above a weak evaporite or overpressured shale substrate, is commonly observed in other fold belts such as the Perdido of the western Gulf of Mexico (Gradmann et al., 2009) or the Zagros belt in Iran (Alavi, 2007).

In the next phase of the kinematic model from ~6.5 to 4.0 Ma, we interpret early fold inflation to drive steepening of the forelimb as the rafted backlimb beam continues to translate downdip (Fig. 2d–e). In this scenario, the base of the forelimb is essentially ‘pinned’ at the seaward limit of the autochthonous salt. In simple kinematic models of these asymmetric folds, significant steepening of the forelimb is often attributed to generating substantial shear strain and drive pervasive deformation band formation (Schultz and Siddharthan, 2005), which in turn can cause significant downdip permeability reduction and flow baffling. In many Gulf of Mexico anticlines, this subseismic strain may limit the usefulness of secondary recovery pressure support strategies such as water injection, as the fluid pressures on the flank of the fold cannot be transmitted updip due to the permeability reduction (Ballas et al., 2015). In both the BC1 and RS2 models, asymmetric fold steepening does not occur at the model time equivalent to the timing of fold steepening in the kinematic model, precluding our ability to examine the strain effects of this process.

Following inflation of the salt and forelimb steepening, the next key phase interpreted from the kinematic restoration is the emplacement of the allochthonous salt canopy coeval with collapse of the fold backlimb (Fig. 2e–g). Based on the interpreted stratigraphic relationships at the downdip toe of the salt sheet, we interpret the emplacement to have occurred over ~3 Myr (4–1 Ma), with further vertical inflationary growth producing the modern Sigsbee escarpment in recent time. Because the finite element model is not kinematically prescribed and is thus essentially a ‘free’ model, it is impossible to predetermine where

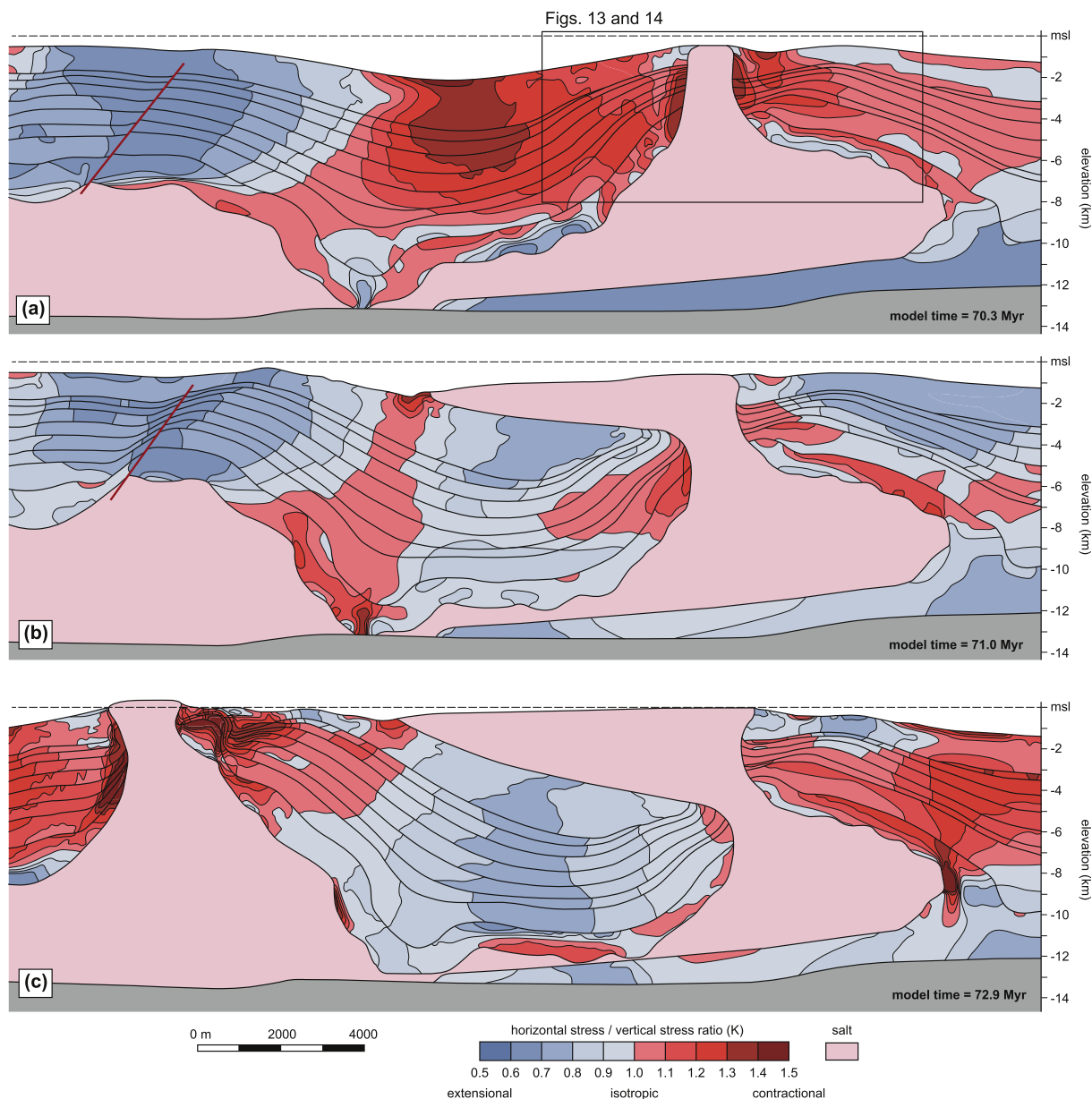


Fig. 12. K (horizontal/vertical stress ratio) condition for the RS2 model during the final stages. (a) At model time 70.3 Myr, the emerging diapir stock creates a strong compressional stress field in the adjacent wall rocks. This is in stark contrast to the updip anticline, which exhibits a broadly extensional stress field over the crest of the fold, likely as a consequence of the clockwise rotation of the common limb between the two major folds. (b) Clockwise rotation and collapse of the common limb allows growth of the downdip salt sheet and enhanced development of an extensional zone over the updip anticline. (c) Emergence of the updip diapir drives a rapid transition from a dominantly extensional stress regime to dominantly compressional regime in the wall rocks adjacent to the diapir. These high K values in the wall rocks adjacent to the diapir presumably reflect compressional deformation occurring in these zones during active diapirism. These results highlight the extreme variation in stress conditions, and particularly the K value, that may occur during different stages of diapir evolution.

such a localized failure may occur. However, the finite element model remains useful for evaluating the validity of the interpreted mechanisms driving structural evolution.

In the Atwater fold belt, the emplacement of the salt sheet occurs updip of the anticline being investigated, but this is not realized in any of the iterations of the finite element model. In the CM1 model, the backlimb of the major anticline does collapse; however, the interplay between the emergent salt flow rates and the rate of deposition limits substantial lateral advance of salt and thus prevents the development of an allochthonous canopy. In the BC1 model, the lack of failure in the overburden prevented the development of diapirism by any mechanism, although the inflation of the nascent anticlines indicated that salt pressure was capable of influencing overburden deformation in the contractional toe of the system. With the reduction of the material

friction angle in the RS2 model, diapirism was able to occur sequentially in both of the major contractional anticlines.

8.2. Reactive v. active mechanisms driving diapirism and salt sheet emergence in fold belts

In the Atwater fold belt, our kinematic interpretation presumes that the major allochthonous salt canopy was emplaced following failure of the thick overburden sequence updip of our anticline of interest. Failure in this case is likely manifested as extensional shearing and/or development of a discrete extensional fault or faults. Thus, to physically and mechanically validate this interpretation, it is necessary to demonstrate that such an event can occur. Fortunately, the finite element model allows us to examine the stress conditions that initiate and sustain

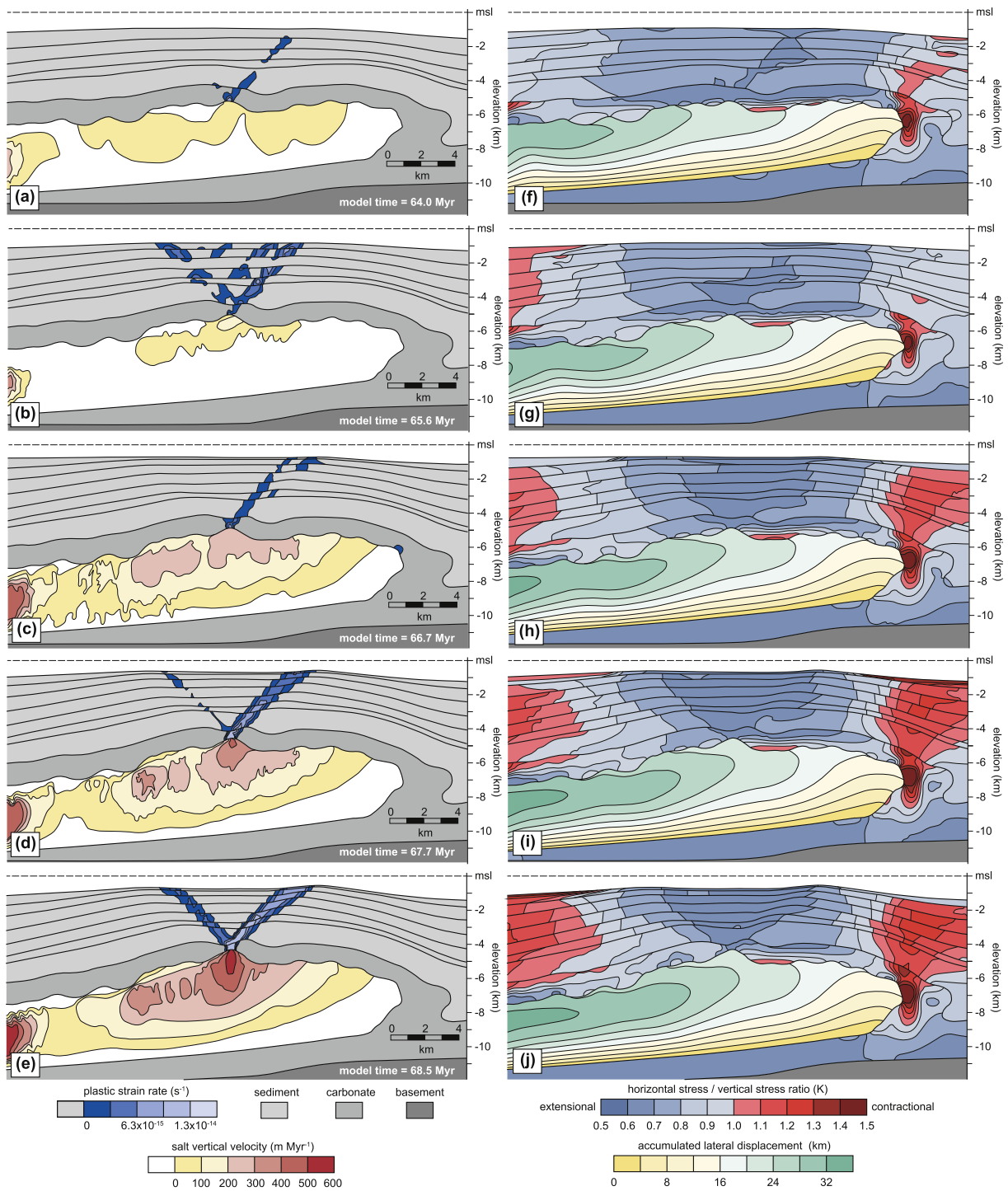


Fig. 13. Results from the RS2 finite element from the time interval (64.0–68.5 Myr) that includes the initiation and early evolution of the major downdip diapir. (a–e) For each time step, the plastic strain rate shows the localization of active deformation in the suprasalt overburden and the vertical velocity of salt records the instantaneous distribution of vertical salt motion. (f–j) The horizontal to vertical stress ratio (K_h) in the suprasalt sequence shows the instantaneous distribution and magnitude of extensional and contractional stress conditions. During the time interval, progressive development of nascent crestal normal faults associated with outer arc extension across the anticlinal crest acts to initiate and focus vertical salt flow, leading to the interpretation that diapirism here is initiated by reactive, rather than active behavior. Following diapir initiation, the rapidly increasing vertical salt flow leads to the establishment of a lateral salt ‘channel’ (accumulated lateral displacement; f–j) that accommodates salt flow over distances > 34 km downdip to supply the emerging diapir.

diapirism and the finite strain that results from this evolution, thus allowing the mechanisms driving diapirism to be resolved. The key lies in recognizing whether or not overburden deformation leads to reactive diapirism or alternately, that salt actively pushes aside the overburden material and thus causes the salt flow to localize.

In the RS2 model, diapirism first occurs in the most downdip

anticline. Subsequent diapirism in the adjacent anticline in the updip direction (to the left in Fig. 11) is actually initiated by extension and collapse of the common limb between the two anticlines, so it is most useful to examine the emergence of the initial diapir as an analogue to development of the Atwater salt sheet. Following initial inflation of the anticline early in the model evolution (6–30 Myr; Fig. 10a) due to

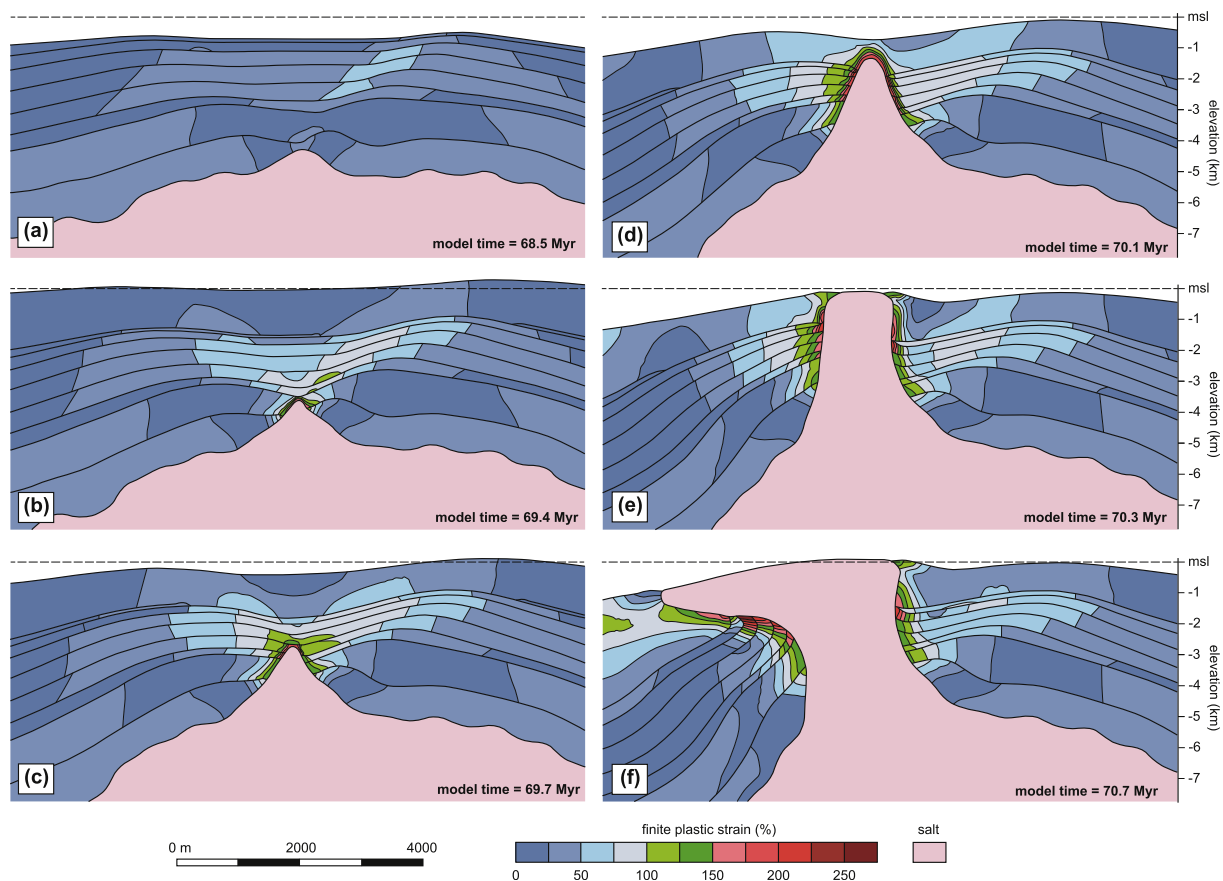


Fig. 14. Finite plastic strain evolution of the downdip diapir in the RS2 model. No vertical exaggeration. (a) At 68.5 Myr, diapirism is still initiating as a consequence of overburden extension, and thus the strain is mostly limited to the left-dipping high strain zone that represents a nascent normal fault developing as part of the crestal graben system. (b–c) From 69.4 to 69.7 Myr, much of the plastic strain continues to concentrate in the graben bounding faults, however very high plastic strain ($> 150\%$) begins to localize near the tip of the emerging salt body, presumably indicating the onset of active salt ‘tunneling’ toward the surface. (d–e) By 70.1 Myr, the geometry of the strain gradient mirrors the geometry of the emerging salt tip and thus appears to indicate that active diapirism is dominating the salt flow through the overburden. Adjacent to the emerging salt, plastic strains up to 200% are recognized and strain values as high as 100% are recognized up to 1.5 km away from the salt-sediment interface. This trend continues as the salt emerges to the surface at 70.3 Myr. (f) Following emergence, the salt begins to rapidly flow in the updip direction and eventually forms the allochthonous salt canopy. High salt flow rates continue to drive both subseismic plastic strain ($> 225\%$) and seismically-resolvable overturned folding of the adjacent wall rocks.

downdip salt flow, the subsalt volume beneath the anticline remains essentially static from 30 to ~ 63 Myr. At ~ 64 Myr, a broad yet weakly developed extensional stress field ($K = 0.7\text{--}0.8$) begins to emerge across the crest of the anticline (Fig. 13a–f); however, no measurable shear strain associated with this stress field is observed in the overburden sequence. From 64 to 65.6 Myr, the extensional stress field becomes more strongly developed ($K \sim 0.6$) and this results in the initial localization of a nascent normal fault on the forelimb of the structure (Fig. 13a–f). At this time, vertical salt flow is limited to slow, diffuse flow beneath the anticline (salt vertical velocity < 0.1 km Myr $^{-1}$; Fig. 13a). At 65.6 Myr, multiple conjugate normal faults begin to form across the crest of the anticline and their formation is accompanied by a progressively increasing vertical salt velocity that begins to localize near the anticlinal crest (Fig. 13b). This behavior continues throughout the early diapir evolution at ~ 68.5 Ma, as the anticlinal crest develops two major conjugate normal faults that create a crestal graben (Fig. 13e). At the base of this crestal graben, vertical salt flow becomes increasingly localized, with velocities > 0.5 km Myr $^{-1}$ observed at this time. This increased vertical flow is accommodated by lateral flow of the salt from the more updip parts of the system into the anticline. By 68.5 Myr, parts of the salt body supporting this volume increase have flowed laterally over distances > 32 km (Fig. 13j), essentially establishing a ‘channel’ that feeds the nascent diapir. Because the crestal extension appears to predate the increased

salt flow rates, we interpret the initial diapir evolution to be reactive. Although reactive mechanisms are most commonly recognized in extensional parts of the salt system, the finite element model clearly shows that such behavior can also occur on the crest of major anticlines in the contractional parts of the system. This observation is critical in that it shows that active mechanisms may not be required to initiate diapirism in fold belts like the Atwater.

8.3. Finite strain path of suprasalt sediment packages and implications for reservoir damage

Despite the recognition that diapirs in contractional zones can initiate due to reactive mechanisms, active diapirism may still play a key role in the creation of accommodation space to sustain salt flow and in generating strain in the wall rocks and cover sequences adjacent to the growing diapir. To determine if active mechanisms were operating, we examined the strain history of the wall rocks during diapir formation (Fig. 14).

In the RS2 model, extension and subsequent reactive diapirism initiates at ~ 64.0 Myr (Fig. 13a), and by 68.5 Myr vertical surface-directed salt flow has ramped up to velocities > 500 m Myr $^{-1}$. From 68.5 to 70.7 Myr, the evolving salt structure advances rapidly from reactive diapir to emergent salt stock to updip flowing salt sheet. At the beginning of this transition period, plastic strain in the overburden is

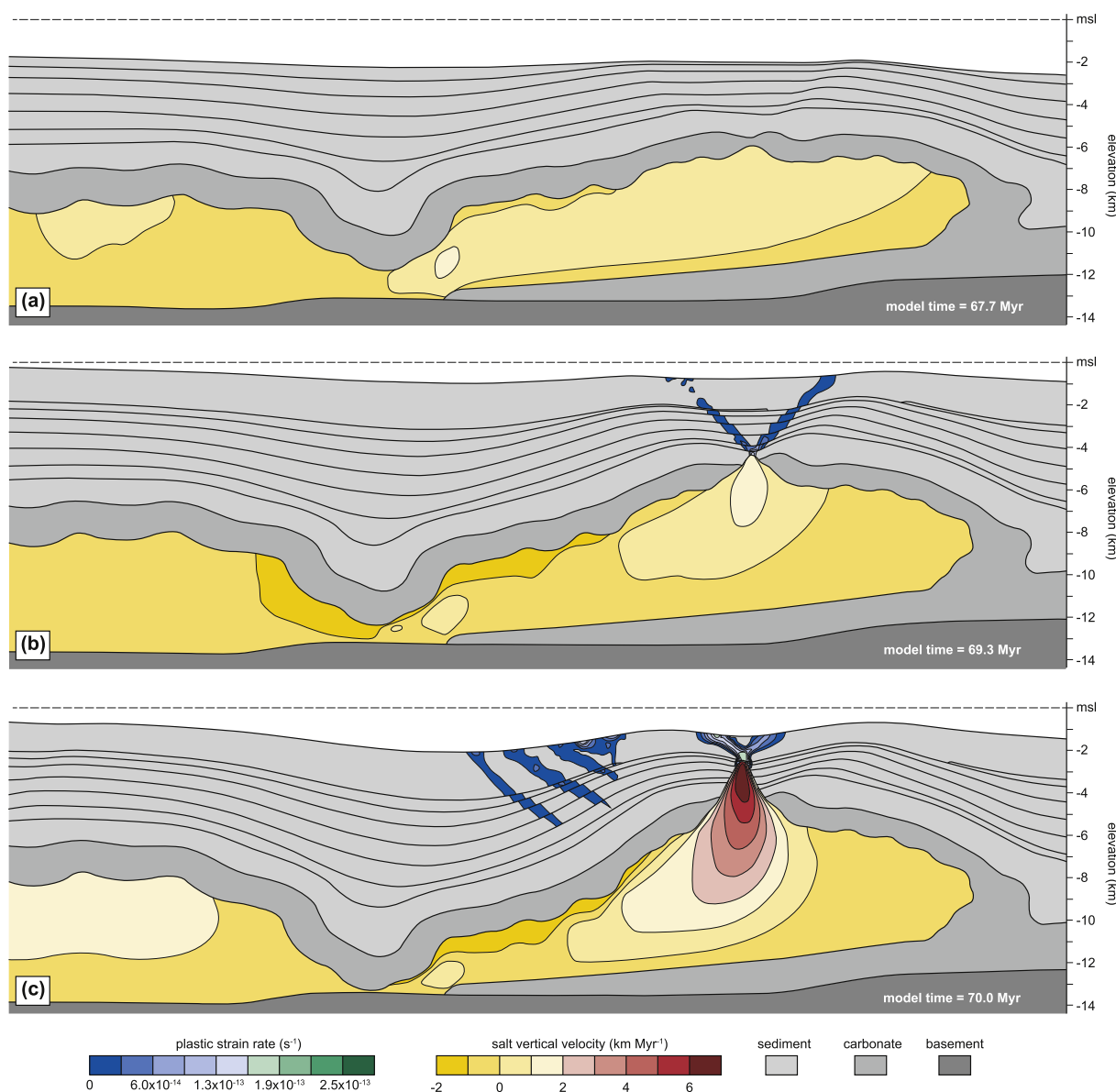


Fig. 15. Plastic strain rate and salt vertical velocity results for the early evolution of the dowdip diapir. Note that scale for both results is different than that used in Fig. 15. No vertical exaggeration. (a) Salt inflation begins to drive early development of the crestal graben but major surface-directed salt flow has not yet localized at 67.7 Myr. (b) Following onset of slip along both crestal graben normal faults, surface-directed salt flow velocity increases ($> 1 \text{ km Myr}^{-1}$) at the base of the graben in response to the overburden extension. (c) Continued extension coupled with active diapirism drives extreme localization of surface directed salt flow, with flow velocities $> 6 \text{ km Myr}^{-1}$ at the emerging salt tip.

mostly limited to the nascent crestal graben faults (Fig. 14a), with cover rocks at the crest of the anticline adjacent to salt yielding plastic strains of $< 50\%$. By 69.4 Myr, however, wall rocks adjacent to the leading tip of the diapir exhibit plastic strain $> 150\%$ and strain $> 75\%$ extends up to 1 km away from the diapir tip (Fig. 14b). At 70.3 Myr, immediately prior to surface emergence of the diapir, the magnitude and distribution of compactional horizontal stress ($K > 1$; Fig. 12a) and plastic strain (Fig. 14d) clearly demonstrates that the diapir is actively ‘tunneling’ through the cover sequence, as the strain gradient identically mirrors the shape of the emerging salt. At that time, plastic strain in the wall rocks immediately adjacent to the tunneling salt approaches 200% and plastic strain $> 100\%$ occurs up to 1 km away from the salt-sediment boundary. As the diapir transitions from stock to sheet (Fig. 14e–f), lateral salt flow causes overturned folding of the wall rock layers to the left of the diapir, in addition to the pervasive plastic strain produced in the wall rocks and folded layers. Substantial plastic strain in these steeply dipping and overturned flaps exceeds 50% up to 2 km away

from the salt-sediment interface and commonly exceeds 200% within 1 km of that boundary. In these systems, this deformation is driven by peak vertical salt flow velocities $> 6 \text{ km Myr}^{-1}$ (Figs. 15 and 16). Because these overturned traps are ideal analogs for the three-way traps that are often targeted by the petroleum industry, the magnitude of plastic strain predicted by our numerical models demonstrates that diapir evolution can produce substantial reservoir damage and consequent flow baffling, possibly in the form of distributed deformation banding (Schultz and Siddharthan, 2005; Fossen et al., 2007). Additionally, recent numerical studies have demonstrated that this strain, which occurs at both the subseismic and seismically-resolvable scale, cannot be accurately restored and thus cannot be predicted using traditional kinematic techniques (Heidari et al., 2017; Nikolinakou et al., 2017).

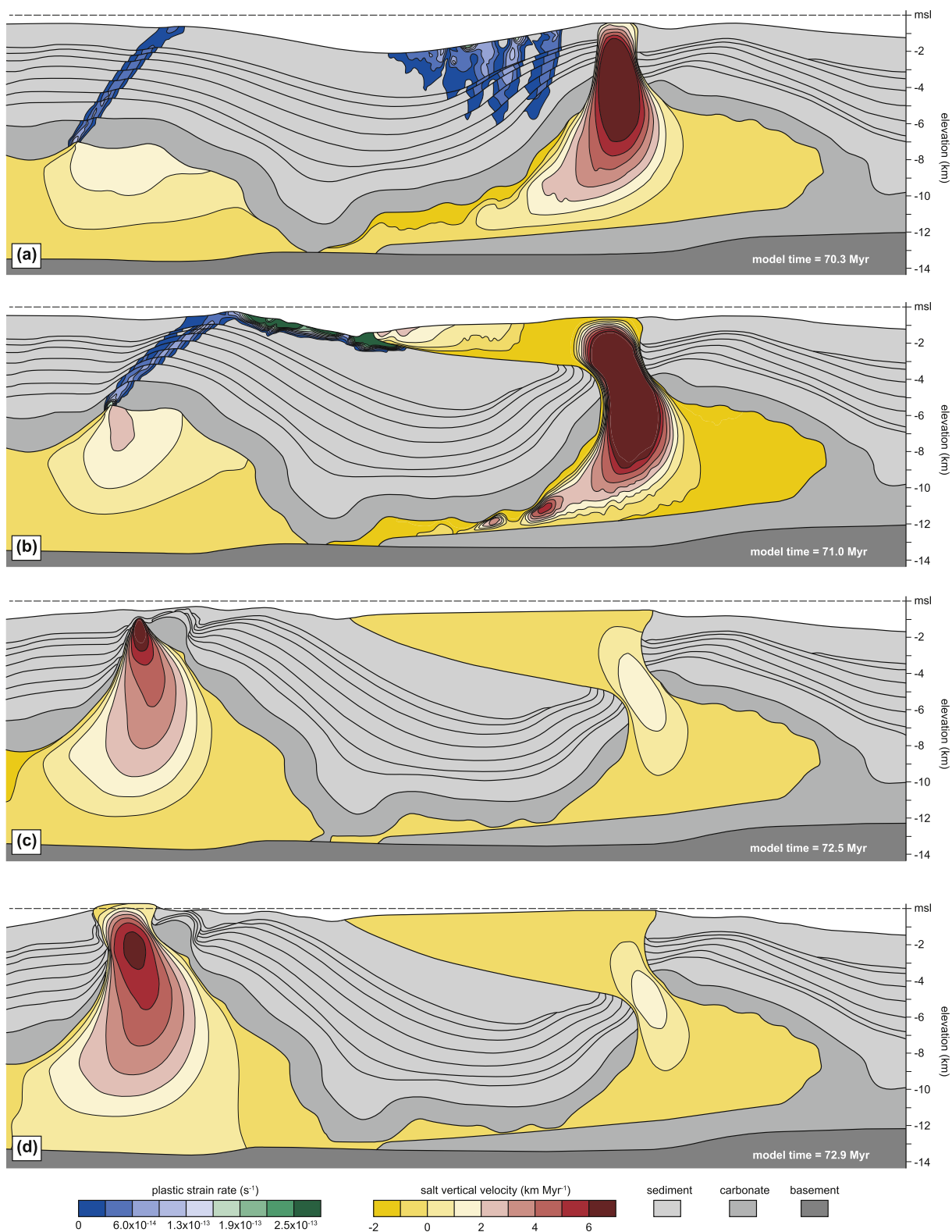


Fig. 16. Plastic strain rate and salt vertical velocity results for the late evolution of the downdip diapir and emergence of the updip diapir. Note that scale for both results is different than that used in Fig. 15. No vertical exaggeration. (a) Once the downdip diapir becomes emergent, the halostatic pressure supporting the downdip anticline is released, causing the common syncline between the anticlines to begin rotating clockwise and foundering. This motion drives the development of a major normal fault at the crest of the updip anticline. (b) With continued rotation of the common syncline, the normal fault at the crest of the updip anticline continues to develop and this extension drives localization of surface-directed salt flow beneath this developing structure. Simultaneously, continued clockwise rotation of the common syncline drives deep salt flow into the downdip diapir and towards the surface while also producing accommodation space at the surface for the development of the allochthonous salt sheet. (c) Continued extension of the overburden above the updip diapir allows vertical salt to accelerate and drive substantial deformation and folding of the overburden. At this time, the common syncline essentially is welded at the base, thus eliminating the pressure driving salt evacuation in the downdip diapir, causing the downdip stock feeder and overlying salt sheet to stabilize. (d) In the final stage of the model, the updip diapir has now become the ‘release valve’ for long wavelength halostatic pressure in this system.

9. Conclusions

Using a case study from the Atwater fold belt, Gulf of Mexico, we evaluate a new workflow that involves comparison of rigorously executed kinematic restorations with simplified forward numerical models of structural evolution to examine the physical validity of derived solutions and to determine the nature and spatial distribution of the resultant subseismic deformation. In the Atwater fold belt, which represents the downdip portion of a linked updip extension-downdip contractional system, our kinematic restorations indicated that major anticlines likely result from early short wavelength folding followed by (1) inflation of the autochthonous salt to drive failure of the overburden, (2) collapse of the major anticlinal backlimb, and (3) rapid emplacement of the allochthonous salt canopy.

In margin-scale finite element models of the same system, progradation of the sedimentary wedge above the weak salt substrate leads to basinward migration of the salt and produces inflation of the major downdip salt-cored folds, as predicted by the kinematic model. However, in relatively strong overburden materials (critical state material, overburden friction angle = 32°), such salt flow only sustains inflation of the anticlines and is unable to reproduce the interpreted collapse of the anticlinal backlimb or emplacement of the salt canopy. Alternate model runs that include a significant reduction in material strength (overburden friction angle = 18°) allow development of diapirism in the anticlinal crest and ultimately lead to rapid emplacement of allochthonous canopies similar to those observed in the Atwater system. A lower frictional strength may be realistic in light of recent experiments on claystones from the deepwater Gulf of Mexico, however it also potentially indicates that overpressure might be significant in reducing effective stress and promoting failure. Nevertheless, in a simplistic sense, one would assume that because these diapirs are forming in the contractional segment of the linked salt system, they would likely initiate due to active diapirism. The numerical models, however, show that overburden failure due to outer arc bending initiates prior to the localization of vertical, surface-directed salt flow. Thus, diapirism in these systems can result from an evolutionary path that includes: (1) anticlinal development due to salt inflation at the toe of the linked salt system, (2) outer arc bending and subsequent overburden extension due to the continued autochthonous salt inflation, and (3) initiation of diapirism as a result of reactive (extensional) mechanisms. Despite the recognition that diapirism in these contractional folds can initiate by reactive mechanisms, the numerical models showed that active diapirism plays a key role in the strain evolution of the mostly unconsolidated wall rocks. In all of these models, diapirism drives substantial seismically-resolvable (overturned folding) and subseismic deformation (> 200% plastic strain) of wall rocks. This deformation is driven by salt ‘tunneling’, as indicated by the pronounced strain gradient geometry that mirrors the boundary of the rising salt.

Finally, these models show that the stress field, and particularly the K value (horizontal-vertical stress ratio) of the sediments adjacent to salt structures used for estimating stress magnitudes for drilling predictions, is fundamentally dependent on where along the evolutionary path from autochthonous salt, to diapir, to salt sheet, that each structure resides. These results highlight the need to test complex kinematic restorations with physics-based techniques. Additionally, they demonstrate that integrating kinematic restorations with these finite element solutions can substantially increase our ability to predict both subseismic reservoir damage in sediments adjacent to salt structures and the K values used for forecasting drilling conditions. This is particularly significant in an exploration context, where the paucity of well data creates a greater necessity to bolster forecasted conditions with geo-mechanical modeling, among other techniques.

Acknowledgements

The authors would like to thank Cynthia Blankenship and Pramod

Singh for their support of this project in the early stages. Critical review comments by Dolores Robinson, Paul Betka, and associate editor Ian Alsop greatly improved a previous version of this manuscript.

Appendix A. Supplementary data

Supplementary data to this article can be found online at <https://doi.org/10.1016/j.jsg.2018.10.003>.

References

- Alavi, M., 2007. Structures of the Zagros fold-thrust belt in Iran. *Am. J. Sci.* 307, 1064–1095. <https://doi.org/10.2475/09.2007.02>.
- Allen, J., Beaumont, C., 2012. Impact of inconsistent density scaling on physical analogue models of continental margin scale salt tectonics. *J. Geophys. Res.* 117, B08103. <https://doi.org/10.1029/2012JB009227>.
- Ballas, G., Fossen, H., Soliva, R., 2015. Factors controlling permeability of cataclastic deformation bands and faults in porous sandstone reservoirs. *J. Struct. Geol.* 76, 1–21. <https://doi.org/10.1016/j.jsg.2015.03.013>.
- Carter, N.L., Hansen, F.D., 1983. Creep of rock salt. *Tectonophysics* 92, 275–333. [https://doi.org/10.1016/0040-1951\(83\)90200-7](https://doi.org/10.1016/0040-1951(83)90200-7).
- Casey, B., Germaine, J.T., Flemings, P.B., Fahy, B.P., 2016. In situ stress state and strength in mudrocks. *J. Geophys. Res.: Solid Earth* 121. <https://doi.org/10.1002/2016JB012855>.
- Christeson, G.L., Van Avendonk, H.J.A., Norton, I.O., Snedded, J.W., Eddy, D.R., Karner, G.D., Johnson, C.A., 2014. Deep crustal structure in the eastern Gulf of Mexico. *J. Geophys. Res.* 119, 6782–6801. <https://doi.org/10.1002/2014JB01145>.
- Crook, A.J.L., Owen, D.R.J., Willson, S., Yu, J., 2006. Benchmarks for the evolution of shear localization with large relative sliding in frictional materials. *Comput. Methods Appl. Mech. Eng.* 195, 4991–5010.
- Crook, T., Willson, S., Yu, J.G., Owen, R., 2003. Computational modeling of the localized deformation associated with borehole breakout in quasi-brittle materials. *J. Petrol. Sci. Eng.* 38, 177–186.
- Demercian, S., Szatmari, P., Cobbold, P.R., 1993. Style and pattern of salt diapirs due to thin-skinned gravitational sliding, Campos and Santos basins, offshore Brazil. *Tectonophysics* 228, 393–433.
- Fredrich, J.T., Coblentz, D., Fossum, A.F., Thorne, B.J., 2003. Stress perturbations adjacent to salt bodies in the deepwater Gulf of Mexico. *Soc. Petrol. Eng.* 84554.
- Fredrich, J.T., Fossum, A.F., Hickman, R.J., 2007. Mineralogy of deepwater Gulf of Mexico salt formations and implications for constitutive behavior. *J. Petrol. Sci. Eng.* 57, 354–374. <https://doi.org/10.1016/j.petrol.2006.11.006>.
- Fossen, H., Schultz, R.A., Shipton, Z.K., Mair, K., 2007. Deformation bands in sandstone: a review. *J. Geol. Soc. Lond.* 164, 755–769.
- Fossum, A.F., Fredrich, J.T., 2002. *Salt Mechanics Primer for Near-salt and Sub-salt Deepwater Gulf of Mexico Field Developments*: Sandia National Laboratories Report SAND2002-2063.
- Galloway, W.E., 2008. Chapter 15: depositional evolution of the Gulf of Mexico sedimentary basin. *Sediment. Basins World* 5. [https://doi.org/10.1016/S1874-5997\(08\)00015-4](https://doi.org/10.1016/S1874-5997(08)00015-4).
- Galloway, W.E., Ganey-Curry, P.E., Li, X., Buffler, R., 2000. Cenozoic depositional history of the Gulf of Mexico basin. *AAPG (Am. Assoc. Pet. Geol.) Bull.* 84, 1743–1774.
- Gemmer, L., Ings, S.J., Medvedev, S., Beaumont, C., 2004. Salt tectonics driven by differential sediment loading: stability analysis and finite-element experiments. *Basin Res.* 16, 199–218. <https://doi.org/10.1111/j.1365-2117.2004.00229.x>.
- Gemmer, L., Beaumont, C., Ings, S.J., 2005. Dynamic modeling of passive margin salt tectonics: effects of water loading, sediment properties and sedimentation patterns. *Basin Res.* 17, 383–402. <https://doi.org/10.1111/j.1365-2117.2005.00274.x>.
- Gradmann, S., Beaumont, C., Albertz, M., 2009. Factors controlling the evolution of the Perdido Fold Belt, northwestern Gulf of Mexico, determined from numerical models. *Tectonics* 28. <https://doi.org/10.1029/2008TC002326>.
- Hanstchel, T., Kauerauf, A.I., 2009. *Fundamentals of Basin and Petroleum Systems Modelling*. Springer, pp. 469.
- Heidari, M., Nikolinaou, M.A., Flemings, P.B., Hudec, M.R., 2017. A simplified stress analysis of rising salt domes. *Basin Res.* 29, 363–376. <https://doi.org/10.1111/br.12181>.
- Hossack, J., 1995. Geometric rules of section balancing for salt structures. In: Jackson, M.P.A., Roberts, D.G., Snelson, S. (Eds.), *Salt Tectonics: a Global Perspective*, vol. 65. AAPG Memoir, pp. 29–40.
- Hudec, M.R., Jackson, M.P.A., 2007. *Terra infirma: understanding salt tectonics*. *Earth Sci. Rev.* 82, 1–28.
- Ings, S.C., Beaumont, C., Gemmer, L., 2004. Numerical modeling of salt tectonics on passive continental margins: preliminary assessment of the effects of sediment loading, buoyancy, margin tilt, and isostasy. In: Post, P.J. (Ed.), *Salt-sediment Interactions and Hydrocarbon Prospectivity: Concepts, Applications and Case Studies for the 21st Century*. Society for Sedimentary Geology, pp. 36–68.
- Jackson, M.P.A., Talbot, C.J., 1986. External shapes, strain rates, and dynamics of salt structures. *Geol. Soc. Am. Bull.* 97, 305–323.
- Jackson, M.P.A., Vendeville, B.C., 1994. Regional extension as geologic trigger for diapirism. *GSA Bull.* 106, 57–73.
- Karig, D.E., Hou, G., 1992. High-stress consolidation experiments and their geologic implications. *J. Geophys. Res.* 97, 2156–2202. <https://doi.org/10.1029/91JB02247>.
- Kneller, B., 1995. Beyond the Turbidite Paradigm: Physical Models for Deposition of

- Turbidites and Their Implications for Reservoir Prediction, vol. 94. Geological Society of London Special Publications, pp. 31–49. <https://doi.org/10.1144/GSL.SP.1995.094.01.04>.
- Letouzey, J., Colletta, B., Vially, R., Chermette, J.C., 1995. Evolution of salt-related structures in compressional settings. In: Jackson, M.P.A., Roberts, D.G., Snelson, S. (Eds.), *Salt Tectonics: a Global Perspective: AAPG Memoir 65*, pp. 41–60.
- Munson, D.E., Dawson, P.R., 1982. A Transient Creep Model for Salt during Stress Loading and Unloading: Sandia Report SAND82-0962.
- Munson, D.E., Dawson, P.R., 1984. Salt constitutive modeling using mechanism maps. In: *Trans Tech Publications, First International Conference on Mechanical Behavior of Salt*, pp. 931–939.
- Nikolinakou, M.A., Flemings, P.B., Hudec, M.R., 2014a. Modeling stress evolution around a rising salt diapir. *Mar. Petrol. Geol.* 51, 230–238. <https://doi.org/10.1016/j.marpetgeo.2013.11.021>.
- Nikolinakou, M.A., Hudec, M.R., Flemings, P.B., 2014b. Comparison of evolutionary and static modeling of stresses around a salt diapir. *Mar. Petrol. Geol.* 57, 537–545. <https://doi.org/10.1016/j.marpetgeo.2014.07.002>.
- Nikolinakou, M.A., Heidari, M., Hudec, M.R., Flemings, P.B., 2017. Initiation and growth of salt diapirs in tectonically stable settings: upbuilding and megaflaps. *AAPG (Am. Assoc. Pet. Geol.) Bull.* 101, 887–905. <https://doi.org/10.1306/09021615245>.
- Peel, F.J., Travis, C.J., Hossack, J.R., 1995. In: Jackson, M.P.A., Roberts, D.G., Snelson, S. (Eds.), *Genetic Structural Provinces and Salt Tectonics of the Cenozoic Offshore U.S. Gulf of Mexico: a Preliminary Analysis*, vol. 65. AAPG Memoir, pp. 153–175.
- Peric, D., Crook, A.J.L., 2004. Computational strategies for predictive geology with reference to salt tectonics. *Comput. Methods Appl. Mech. Eng.* 193, 5195–5222. <https://doi.org/10.1016/j.cma.2004.01.037>.
- Pfiffner, O.A., Ramsay, J.G., 1982. Constraints on geologic strain rates: arguments from finite strain states of naturally deformed rocks. *J. Geophys. Res.* 87, 311–321.
- Pilcher, R.S., Kilsdonk, B., Trude, J., 2011. Primary basins and their boundaries in the deep-water northern Gulf of Mexico: origin, trap types, and petroleum system implications. *AAPG (Am. Assoc. Pet. Geol.) Bull.* 95, 219–240. <https://doi.org/10.1306/06301010004>.
- Rowan, M.G., Ratliff, R.A., 2012. Cross-section restoration of salt-related deformation: best practices and potential pitfalls. *J. Struct. Geol.* 41, 24–37.
- Rowan, M.G., 1993. Structural styles and evolution of allochthonous salt, central Louisiana outer shelf and upper slope. In: Jackson, M.P.A., Roberts, D.G., Snelson (Eds.), *Salt Tectonics: a Global Perspective: AAPG Memoir 65*, pp. 199–228.
- Rowan, M.G., Peel, F.J., Vendeville, B.C., 2003. Gravity-driven fold belts on passive margins. In: McClay, K.R. (Ed.), *Thrust Tectonics and Hydrocarbon Systems. AAPG Memoir*. <https://doi.org/10.1306/M82813C9>.
- Schultz, R.A., Siddharthan, R., 2005. A general framework for the occurrence and faulting of deformation bands in porous granular rocks. *Tectonophysics* 411, 1–18. <https://doi.org/10.1016/j.tecto.2005.07.008>.
- Spiers, C.J., Urai, J.L., Lister, G.S., Boland, J.N., Zwart, H.J., 1986. The Influence and Fluid-rock Interaction on the Rheology of Salt Rock: Nuclear Science and Technology EUR 10399 EN. Office for official publications of the European Communities, Luxembourg.
- Spiers, C.J., Carter, N.L., 1998. Microphysics of rocksalt flow in nature. In: Aubertin, M., Hardy, H.R. (Eds.), *The Mechanical Behavior of Salt: Proceedings of the Fourth Conference Series on Soil and Rock Mechanics*, vol. 22. pp. 115–128.
- Tang, C.A., Tham, L.G., Lee, P.K.K., Yang, T.H., Li, L.C., 2002. Coupled analysis of flow, stress and damage (FSD) in rock failure. *Int. J. Rock Mech. Min. Sci.* 39, 477–489.
- Thornton, D.A., Crook, A.J.L., 2014. Predictive modeling of the evolution of fault structure: 3-D modeling and coupled geomechanical/flow simulation. *Rock Mech. Eng.* 47, 1533–1549.
- Urai, J.L., Spiers, C.J., Zwart, H.J., Lister, G.S., 1986. Water weakening effects in rocksalt during long term creep. *Nature* 324, 554–557.
- van Keken, P.E., Spiers, C.J., van den Berg, A.P., Muylert, E.J., 1993. The effective viscosity of rock salt: implementation of steady-state creep laws in numerical models of salt diapirism. *Tectonophysics* 225, 457–476.
- Wawersik, W.R., Zeuch, D.H., 1986. Modeling and mechanistic interpretation of creep of rock salt below 200°C. *Tectonophysics* 121, 125–152.
- Weller, J.M., 1959. Compaction of sediments. *AAPG Bull.* 43, 273–310.
- Wu, S.A., Bally, A.W., Cramez, C., 1990. Allochthonous salt structure and stratigraphy of the northeastern Gulf of Mexico, part II, structure. *Mar. Petrol. Geol.* 7, 334–370.